#### **OPEN ACCESS**



# Evidence for an Interaction between the Galactic Center Clouds M0.10–0.08 and M0.11–0.11

Natalie O. Butterfield 1,2 , Cornelia C. Lang 3, Adam Ginsburg 4 , Mark R. Morris 5 , Jürgen Ott 6 , and Dominic A. Ludovici 7 
National Radio Astronomy Observatory, 520 Edgemont Road, Charlottesville, VA 22903, USA; nbutterf@nrao.edu

2 Department of Physics, Villanova University, 800 E. Lancaster Avenue, Villanova, PA 19085, USA

3 Department of Physics and Astronomy, University of Iowa, 30 North Dubuque Street, Iowa City, IA 52242, USA

4 Department of Astronomy, University of Florida, P.O. Box 112055, Gainesville, FL 32611, USA

5 Department of Physics & Astronomy, University of California, 430 Portola Plaza, Los Angeles, CA 90095, USA

6 National Radio Astronomy Observatory, 1003 Lopezville Road, Socorro, NM 87801, USA

7 Department of Physics and Engineering Science, Coastal Carolina University, 100 Chanticleer Drive E, Conway, SC 29528, USA

Received 2021 September 16; revised 2022 August 2; accepted 2022 August 3; published 2022 September 14

#### **Abstract**

We present high-resolution ( $\sim 2-3''$ ;  $\sim 0.1$  pc) radio observations of the Galactic center cloud M0.10–0.08 using the Very Large Array at *K* and *Ka* band ( $\sim 25$  and 36 GHz). The M0.10–0.08 cloud is located in a complex environment near the Galactic center Radio Arc and the adjacent M0.11–0.11 molecular cloud. From our data, M0.10–0.08 appears to be a compact molecular cloud ( $\sim 3$  pc) that contains multiple compact molecular cores (5+; <0.4 pc). In this study, we detect a total of 15 molecular transitions in M0.10–0.08 from the following molecules: NH<sub>3</sub>, HC<sub>3</sub>N, CH<sub>3</sub>OH, HC<sub>5</sub>N, CH<sub>3</sub>CN, and OCS. We have identified more than sixty 36 GHz CH<sub>3</sub>OH masers in M0.10–0.08 with brightness temperatures above 400 K and 31 maser candidates with temperatures between 100 and 400 K. We conduct a kinematic analysis of the gas using NH<sub>3</sub> and detect multiple velocity components toward this region of the Galactic center. The bulk of the gas in this region has a velocity of 51.5 km s<sup>-1</sup> (M0.10–0.08) with a lower-velocity wing at 37.6 km s<sup>-1</sup>. We also detect a relatively faint velocity component at 10.6 km s<sup>-1</sup> that we attribute to being an extension of the M0.11–0.11 cloud. Analysis of the gas kinematics, combined with past X-ray fluorescence observations, suggests M0.10–0.08 and M0.11–0.11 are located in the same vicinity of the Galactic center and could be physically interacting.

Unified Astronomy Thesaurus concepts: Galactic center (565); Interstellar medium (847); Molecular clouds (1072)

#### 1. Introduction

The central 200 pc of the galaxy (Central Molecular Zone; CMZ) is an extreme Galactic environment. Molecular clouds in the CMZ have hotter average gas temperatures (50-300 K; Mauersberger et al. 1986; Mills & Morris 2013; Ginsburg et al. 2016; Krieger et al. 2017), higher densities (10<sup>3-5</sup> cm<sup>-3</sup>; Zylka et al. 1992; Mills et al. 2018a), and broader line widths, on the  $\sim$ 10 pc scale ( $\sim$ 20–30 km s<sup>-1</sup>; Bally et al. 1987; Kauffmann et al. 2017), than typical clouds in the interstellar medium (ISM) of the Galactic disk. The velocities of CMZ clouds range from -250 to +250 km s<sup>-1</sup> within the inner 1°.5 of our Galactic center. The large velocity range of these clouds, wide velocity dispersions, and line-of-sight confusion from multiple velocity components can make it difficult to place individual molecular clouds within the three-dimensional context of the CMZ. Figure 1 shows the inner 100 pc of the Galactic center, where many of these dense molecular clouds are shown in red in this three-color image. Recent efforts have been made to connect these individual clouds (1–10 pc) to the larger structures ( $\sim$ 100 pc) in the Galactic center (Sofue 1995; Sawada et al. 2004; Molinari et al. 2011; Kruijssen et al. 2015; Henshaw et al. 2016).

The three-dimensional orientation of the large-scale structures in the CMZ can depend greatly on the interpretation of the gas kinematics. For example, Sofue (1995) and Sawada et al. (2004) suggest a two-spiral-arm structure, whereas Molinari et al. (2011)

Original content from this work may be used under the terms of the Creative Commons Attribution 4.0 licence. Any further distribution of this work must maintain attribution to the author(s) and the title of the work, journal citation and DOI.

argue for a twisted elliptical ring. The most recent orbital model, presented in Kruijssen et al. (2015), suggests an open-orbit solution (see dashed line in Figure 1 for the projected trajectory of their orbital model solution). In the Kruijssen et al. (2015) orbital model, gas in the CMZ traces an open orbit set by the shape of the CMZ potential. Connected chains of molecular clouds all follow the same orbital path or "stream." The three-dimensional arrangement of clouds along a continuous stream can be loosely reconstructed from their projected radial distance to Sgr A\* and the observed line-ofsight velocity. However, there is still some ambiguity about whether certain features are located on the near or far sides of the Galactic center. Additionally, multiple components along the same line of sight can make it challenging to disentangle the kinematics of a single cloud. High-spatial- and high-spectral-resolution observations targeting regions where the kinematics are complex are needed to resolve the individual components.

One region of the CMZ where the kinematics are complex is toward the M0.10–0.08 molecular cloud (solid white circle in Figure 1). The M0.10–0.08 cloud and the adjacent M0.11–0.11 cloud (annotated in Figure 1) have been observed in several large-scale surveys of molecular gas in the CMZ for many decades (Güsten et al. 1981; Tsuboi et al. 1997; Chuss et al. 2003; Handa et al. 2006; Jones et al. 2012; Mills & Battersby 2017; Battersby et al. 2020; Hatchfield et al. 2020; Guan et al. 2021). Several of the low-spatial-resolution surveys of cold dust and molecular gas show that the M0.10–0.08 cloud is relatively bright and compact (<3 pc), with a mass of  $1.7 \times 10^5$   $M_{\odot}$  (e.g., Tsuboi et al. 2011). The M0.10–0.08 cloud has also been observed to have a substructure, as detected in the recent 1 mm CMZoom survey (Battersby et al. 2020; Hatchfield et al. 2020). M0.11–0.11, however, is relatively faint and extended

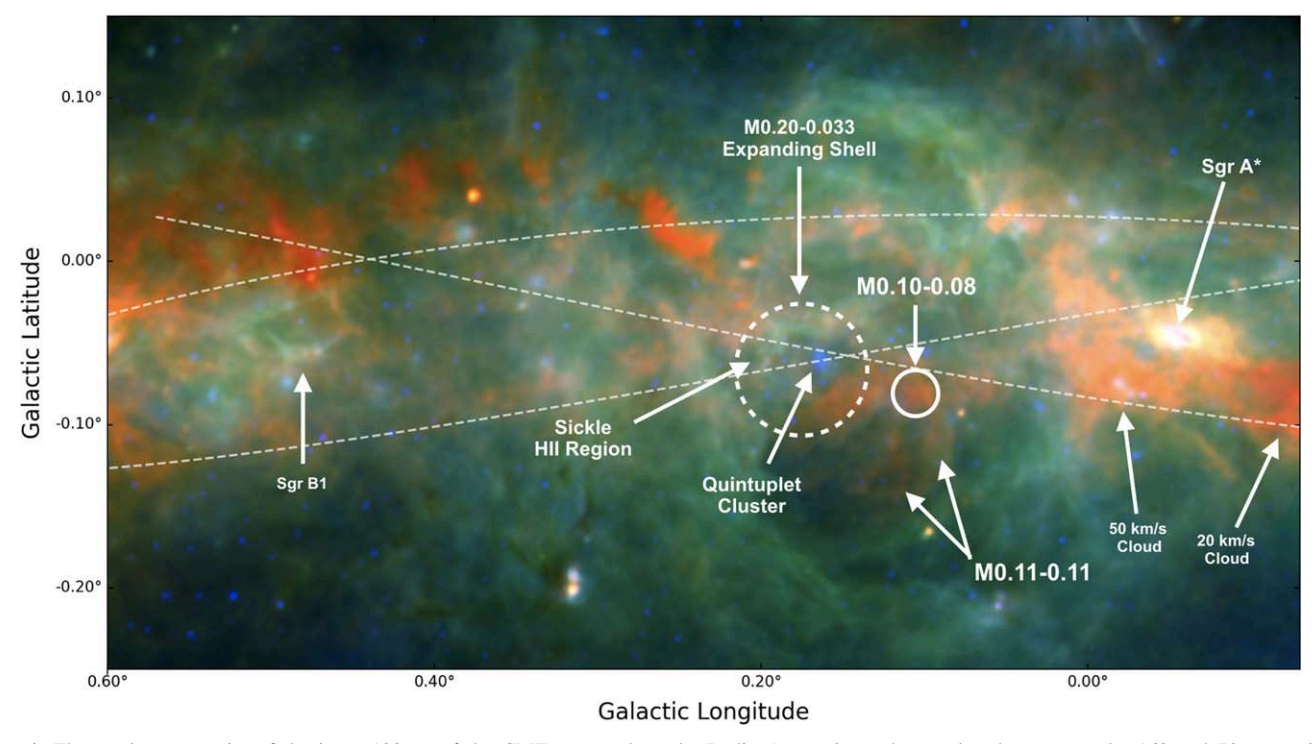


Figure 1. Three-color composite of the inner 100 pc of the CMZ, centered on the Radio Arc region, where red and green are the 160 and 70  $\mu$ m emission, respectively, from HiGAL (Molinari et al. 2010), and blue is the 8  $\mu$ m emission from Spitzer (Churchwell et al. 2009). The solid white circle shows the region of the CMZ targeted in this study. This field is centered on the M0.10–0.08 molecular cloud but could overlap with some of the extended emission in M0.11–0.11. The dashed white circle shows the location of the M0.20–0.033 expanding shell presented in Butterfield et al. (2018). Additional prominent CMZ regions are labeled for reference purposes. Overlaid on this figure is a dashed line showing the extent of the orbital stream proposed by Kruijssen et al. (2015).

(>5 pc) and could spatially overlap with M0.10–0.08 (Figure 1). The spatial overlap between the two clouds has led some investigators to argue for a possible connection between the two clouds (Handa et al. 2006; Clavel et al. 2013). However, there are unsolved questions about this connection in the literature due to the large velocity separation between the two clouds along this line of sight ( $\Delta \nu \sim 30~{\rm km~s^{-1}}$ ; Ponti et al. 2010; Kruijssen et al. 2015). Understanding the connection or separation of the two clouds can give insight into the complex kinematics in the region. Furthermore, disentangling the complex kinematics into a somewhat simple solution is essential for understanding the three-dimensional structure of the gas and the effects that cloud–cloud interactions can have on the gas motions.

We present high-resolution ( $\sim$ 2"-3") radio observations of M0.10 -0.08 using the National Science Foundation's Karl G. Jansky Very Large Array (hereafter VLA). Using these observations, we analyze the morphological and kinematic structure of M0.10-0.08 at high resolution (Section 3) and discuss the relationship of M0.10-0.08 to other clouds in the region (Section 4).

#### 2. Observations and Data Calibration

The observations presented in this paper were taken with the VLA interferometric radio telescope, operated by the National Radio Astronomy Observatory. These VLA observations were part of a larger survey of molecular clouds in the CMZ (PI: Elisabeth A.C. Mills; Project code: 11B-210). This survey

used the K- (18.0–26.5 GHz) and Ka-band (26.5–40.0 GHz) receivers on 2012 January 14 and 13, respectively, with the DnC hybrid array. In this survey we observed 15 spectral lines from several regions in the CMZ. The image cube parameters for all 15 lines are reported in Table 1. The results presented in this paper focus on a single pointing containing M0.10–0.08, <sup>10</sup> centered at  $\alpha(2000) = 17^{\rm h}46^{\rm m}09^{\rm s}79$ ,  $\delta(2000) = -28^{\circ}53'18''.0$ , for the K band, and  $\alpha(2000) = 17^{\rm h}46^{\rm m}11^{\rm s}.37$ ,  $\delta(2000) = -28^{\circ}53'24''.3$ , for the Ka band, with a time on source of  $\sim$ 25 minutes in each frequency band.

The correlator setup for this survey is described in Mills et al. (2015) and Butterfield et al. (2018). High-frequency VLA procedures were used for calibration and imaging, as described in Mills et al. (2015), with one difference. We employed the CLEAN parameter "multiscale" for all spectral lines that had a signal-to-noise ratio >15 and a peak intensity >20 mJy beam (see Table 1) in order to improve our sensitivity to data taken with short baselines in our interferometric observations.

#### 3. Results

#### 3.1. Morphology of the Molecular Emission in M0.10-0.08

Figure 2 presents the peak intensity emission of 11 molecular transitions detected in M0.10–0.08 (see Table 1 for imaging parameters). The remaining four detected molecular transitions in M0.10–0.08 are relatively faint ( $<9\sigma$ ) and

<sup>&</sup>lt;sup>8</sup> The National Radio Astronomy Observatory is a facility of the National Science Foundation operated under cooperative agreement by Associated Universities, Inc.

<sup>&</sup>lt;sup>9</sup> Results from this survey have also been presented in Mills & Morris (2013), Mills et al. (2014, 2015); Ludovici et al. (2016); Butterfield et al. (2018); Mills et al. (2018b).

 $<sup>\</sup>overline{^{10}}$  All J < 7 NH<sub>3</sub> images, shown in Figure 2, are from a larger multipointing mosaic (see Figure 3, left, in Butterfield et al. 2018).

<sup>11</sup> casaguides.nrao.edu/index.php?title=EVLA\_high\_frequency\_Spectral\_Line\_tutorial\_-\_IRC%2B10216\_part1. All imaging and calibration of the VLA observations presented here used the Common Astronomy Software Application (CASA) program provided by NRAO (McMullin et al. 2007).

Table 1
Spectral Line Imaging Parameters for the 15 Molecular Transitions Detected in this Study

			Restoring Beam	n <sup>a</sup>				
Species and Transition	Rest Frequency (GHz)	Major Minor Axis Axis (") (")		Position Angle (°)	Velocity Resolution (km s <sup>-1</sup> )	rms Per Channel (mJy beam <sup>-1</sup> )	Peak Intensity (mJy beam <sup>-1</sup>	
NH <sub>3</sub> (1,1)	23.69450	2.81	2.62	-81.85	1.58	1.3	57.6	
$NH_3(2,2)$	23.72263	2.79	2.62	-85.45	1.58	1.4	56.3	
$NH_3(3,3)$	23.87013	2.77	2.60	-85.18	3.14	2.3	485.9	
$HC_5N (9-8)$	23.96390	3.00	3.00	0.00	3.13	0.8	6.4	
NH <sub>3</sub> (4,4)	24.13942	2.79	2.59	89.49	3.10	1.0	42.0	
OCS $(2-1)^{b,c}$	24.32593	5.00	5.00	0.00	3.08	1.2	8.6	
NH <sub>3</sub> (5,5)	24.53299	2.74	2.55	-90.00	3.05	0.8	28.3	
$CH_3OH (6_2-6_1)^{b,c}$	25.01812	3.00	3.00	0.00	3.00	0.8	5.6	
NH <sub>3</sub> (6,6)	25.05603	2.63	2.48	89.48	2.99	0.9	29.4	
NH <sub>3</sub> (7,7)	25.71518	2.58	2.40	-83.33	2.91	0.7	11.8	
$HC_3N(3-2)$	27.29429	3.14	2.52	16.76	2.75	2.2	55.2	
$NH_3 (9,9)^c$	27.47794	2.80	2.45	43.30	2.73	2.0	16.8	
$CH_3OH(4_{-1}-3_0)$	36.16927	1.95	1.81	-174.63	1.05	$2.9 (50)^{d}$	46969.0	
$HC_3N(4-3)$	36.39232	1.98	1.81	-3.02	2.06	2.8	47.0	
$CH_3CN(2-1)^b$	36.79547	3.00	3.00	0.00	1.02	4.3	40.7	

#### Notes

are therefore not shown in Figure 2. In the following sections, we examine the bright, diffuse molecular emission (Section 3.1.1: NH<sub>3</sub> and HC<sub>3</sub>N). We focus on the kinematics of the NH<sub>3</sub> emission and fit the averaged gas profile in Section 3.2. The CH<sub>3</sub>OH  $(4_{-1}-3_0)$  class I maser transition is discussed in detail in Section 3.3.

#### 3.1.1. Morphology of the Diffuse Molecular Emission: NH<sub>3</sub> and HC<sub>3</sub>N

The top two rows in Figure 2 show the detected  $NH_3$  (1,1) -(7,7) emission in M0.10-0.08. The distribution of the metastable  $NH_3$  emission is similar across all seven transitions. The speckled morphology observed in the  $NH_3$  (7,7) transition is likely an artifact of cleaning with delta functions (see Section 2 and Table 1 for a discussion on the cleaning process).

Most of the NH<sub>3</sub> emission in the M0.10–0.08 cloud is concentrated within a square arcminute region near the center of the field. At high resolution (3"), the M0.10-0.08 cloud has a wedge-like appearance that is narrow at lower Galactic longitude (10''; l = 0.095) and widens with increasing Galactic longitude (50''; l = 0.11). This wedge-like structure is also noticeable in both transitions of  $HC_3N$ : 3–2 and 4–3 (bottom row in Figure 2). Additionally, there is a diffuse "filamentary extension" toward the southern region of M0.10-0.08, as indicated in the bottom rightmost panel of Figure 2 (i.e., the "Features" panel). This filamentary extension is detected in both the NH3 and  $HC_3N$  transitions, but not in the  $CH_3OH(4-3)$  transition. The longest extent of M0.10–0.08 is 75'' ( $\sim 3$  pc), indicating that this cloud is among the more compact molecular clouds observed in the Galactic center (diameters of 3–10 pc; e.g., Güsten et al. 1981; Bally et al. 1987; Kauffmann et al. 2017; Mills & Battersby 2017).

Within M0.10–0.08, there are several ( $\sim$ 5) compact clumps (D < 10'') of brighter NH<sub>3</sub> emission (>0.2 Jy beam<sup>-1</sup>) that are most prominent in the (3,3) transition. Most of these compact clumps are concentrated toward the northeast region of the cloud, with the brightest NH<sub>3</sub> clump located at  $\alpha(2000) =$ 

 $17^{\rm h}46^{\rm m}12^{\rm s}3$ ,  $\delta(2000) = -28^{\circ}53'18''$ . The brightest clump (i.e., "Main Clump"; see "Features" panel in Figure 2) contains emission in all 11 transitions shown in Figure 2, including the fainter CH<sub>3</sub>CN (2–1) transition. Further, the Main Clump is the only location where we detect CH<sub>3</sub>CN emission. Directly south of the Main Clump is a lower-intensity emission region ("Depression"; labeled in the Features panel of Figure 2). This depression region is  $\sim 10''$  across and is located at  $\alpha(2000) = 17^{\rm h}46^{\rm m}12^{\rm s}.5$ ,  $\delta(2000) = -28^{\circ}53'25''$ . The Depression is detected in both NH<sub>3</sub> and HC<sub>3</sub>N but is most prominent in the HC<sub>3</sub>N (4–3) transition. Although this feature is detected in all of our extended emission lines (NH<sub>3</sub>, HC<sub>3</sub>N), it could be produced by spatial filtering in our interferometer data. Future observations at different wavelengths are necessary to determine whether the Depression is some kind of cavity.

#### 3.2. Kinematics of the NH<sub>3</sub> Emission

Figure 3 shows the centroid velocity distribution (moment 1) of the NH<sub>3</sub> (3,3) transition. Most of the bright NH<sub>3</sub> emission (>10 $\sigma$ ) is at a velocity of 35–65 km s<sup>-1</sup>. However, as we will show in the following section, faint (<10 $\sigma$ ) molecular emission is detected at lower velocities of ~10 km s<sup>-1</sup>.

We note an asymmetry in the velocity distribution that results in roughly a 10 km s<sup>-1</sup> pc<sup>-1</sup> gradient (where 1 pc is ~25"). Most of the higher-velocity NH<sub>3</sub> (3,3) emission ( $v \ge 55$  km s<sup>-1</sup>) is located toward the northwestern side of M0.10–0.08 (around  $b = -0^{\circ}.075$ ), and the lower-velocity emission ( $v \le 45$  km s<sup>-1</sup>) is generally located toward the south and southeastern sides of M0.10–0.08 (around  $b = -0^{\circ}.09$ ). The orientation of the described velocity gradient is perpendicular to the direction of

<sup>&</sup>lt;sup>a</sup> Where 1" is 0.04 pc at an assumed distance of 7.9 kpc to the CMZ (Do et al. 2019).

<sup>&</sup>lt;sup>b</sup> These four transitions were smoothed from the natural spatial resolution to improve the signal-to-noise ratio.

<sup>&</sup>lt;sup>c</sup> These four transitions had a signal-to-noise ratio < 9 and are therefore not shown in Figure 2.

<sup>&</sup>lt;sup>d</sup> The larger value in parentheses is the rms noise in the channel containing the brightest maser, at v = 50.6 km s<sup>-1</sup>.

 $<sup>\</sup>overline{^{12}}$  There is a second lower-level emission region to the west of the Main Clump and north of the Filamentary Extension (see Figure 2). However, because we detect emission above the noise level in this region in the  $HC_3N$  (4–3) transition, we do not characterize this feature as a second "depression."

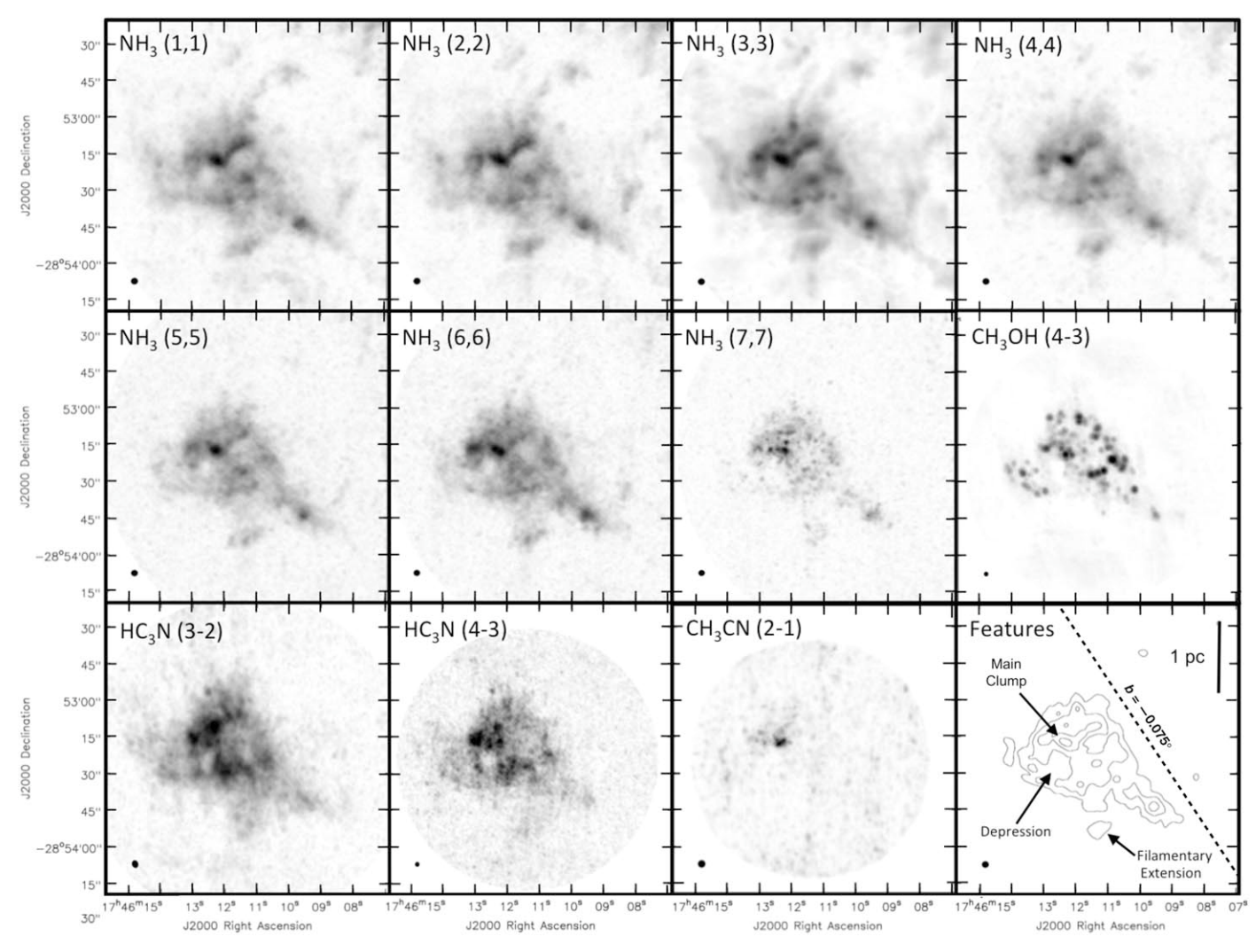
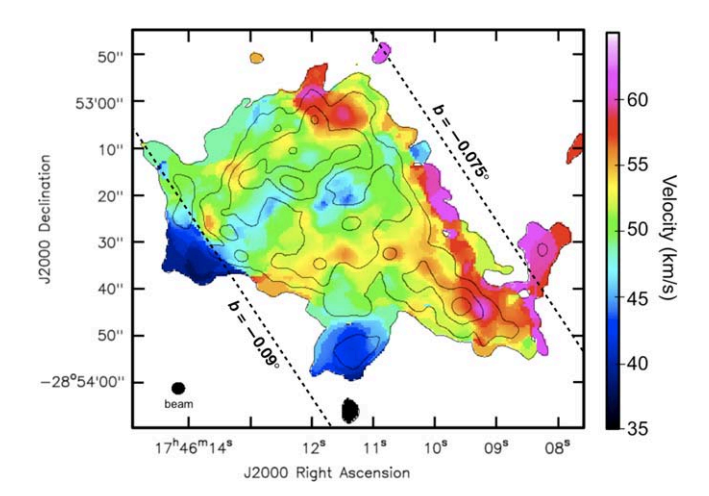


Figure 2. Peak intensity distribution of 11 of the 15 molecular line transitions detected in this paper. The top two rows show the NH<sub>3</sub> (1,1)–(7,7) and CH<sub>3</sub>OH line emission. The bottom row shows the observed HC<sub>3</sub>N and CH<sub>3</sub>CN transitions. The bottom rightmost panel shows the  $20\sigma$ ,  $40\sigma$ ,  $80\sigma$ , and  $140\sigma$  contour levels of the NH<sub>3</sub> (3,3) emission, with annotations identifying several of the "Features" discussed in Section 3.1.1. The spatial resolution of each presented molecular transition is shown in the bottom-left corner of every panel. The imaging parameters of all 15 detected molecular transitions are described in Table 1. The black dashed line shows the orientation of the Galactic plane at b = -0.0075.



orbital motion in the Kruijssen et al. (2015) orbital model. The filamentary extension, described in Section 3.1, contains mainly lower-velocity emission (35–45 km s<sup>-1</sup>) and is oriented roughly parallel to the described velocity gradient.

#### 3.2.1. Multiple Velocity Components toward M0.10-0.08

Moment 1 maps, like the one presented in Figure 3, have the advantage of showing the predominant velocity distribution across a cloud or region. However, these maps can be misleading because they can average over multiple components and be weighted by the brighter emission components. Integrating the emission across a cloud or region, and analyzing the spectra using fitting programs like pyspeckit (Ginsburg & Mirocha 2011; Ginsburg et al. 2022)<sup>13</sup> can help identify and distinguish multiple components. Once these velocity components are disentangled, we can map their spatial distribution and morphology by isolating channels associated with the individual velocity component. By analyzing the gas kinematics using numerous methods we

<sup>13</sup> The pyspeckit Python program is available online at https://github.com/pyspeckit/pyspeckit.

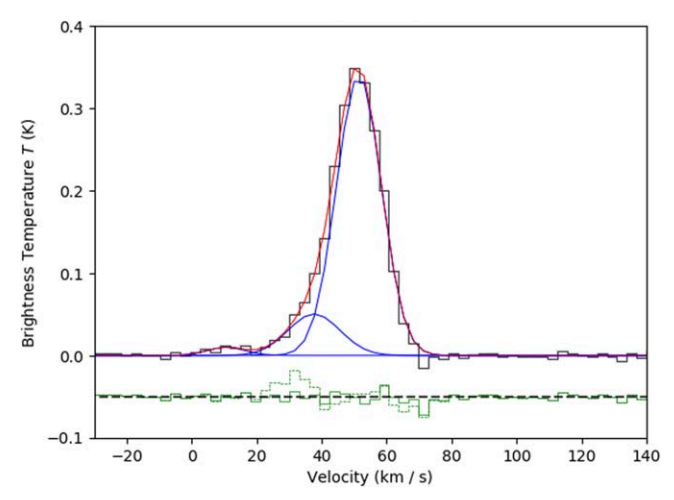


**Figure 4.** NH<sub>3</sub> (5,5) velocity spectrum averaged over the entire field of view. The NH<sub>3</sub> (5,5) line was chosen as a representative spectrum to show the multiple components toward this region. In the (5,5) line, all three components are detected and at this higher *J* transition, the hyperfine lines are suppressed. The black line shows the data. The blue Gaussians show the individual components (presented in Table 2), with the red line showing the sum of the three Gaussian components. The solid green line at -0.05 K shows the residuals of the three-Gaussian-component fit. The dashed green line at -0.05 K shows the residuals of a two-Gaussian-component fit ( $v_c \simeq 10 \text{ km s}^{-1}$  and 50 km s<sup>-1</sup>). In the two-Gaussian fit, there is consistent excess of emission around  $\sim 20-40 \text{ km s}^{-1}$  (six spectral cube channels; dashed green line). This excess emission around  $20-40 \text{ km s}^{-1}$  is brighter than the emission in the 10.6 km s<sup>-1</sup> component and is detected in the HC<sub>3</sub>N transitions as well. Therefore, we interpret the excess emission as an intermediate-velocity component.

can understand the relative structure of the two clouds toward this complex region. In this section, we will identify the velocity components toward the M0.10-0.08 cloud by analyzing the  $NH_3$  (5,5) line.

Figure 4 shows the raw integrated spectrum (black histogram) of the NH<sub>3</sub>(5,5) line. We chose to analyze the J=5NH<sub>3</sub> transition because the hyperfine satellite lines are quite weak and do not contribute significantly to the spectrum. We initially fit the NH<sub>3</sub>(5,5) line with two main Gaussian components at  $\sim 10-15$  km s<sup>-1</sup> and  $\sim 50-55$  km s<sup>-1</sup>. The residuals from this initial fit showed an excess around 20-40 km s<sup>-1</sup> (dashed green line; Figure 4). This excess emission, which appears as a lowervelocity wing to the brighter  $\sim 50-55$  km s<sup>-1</sup> velocity component, is detected in nearly all of our observed lines (e.g., NH<sub>3</sub>, HC<sub>3</sub>N). Because this excess is detected in multiple molecules and transitions, we interpret it to be an intermediate-velocity component. Including a third component in our fitting process greatly reduced the residuals to produce the solid green residual in Figure 4. The final fit parameters used to produce the three Gaussian components in Figure 4 are listed in Table 2.

The lowest-velocity component, which has a central velocity of  $10.6 \text{ km s}^{-1}$ , is the faintest of the three components. This velocity component is detected in both the HC<sub>3</sub>N transitions and in the NH<sub>3</sub> lower J transitions (J<7). The highest-velocity component, fit with a central velocity of  $51.5 \text{ km s}^{-1}$ , is the brightest of the three components and is detected in all of our observed molecular lines. This velocity component appears to dominate the moment 1 map, shown in Figure 3. The intermediate-velocity component, which is best fit with a central velocity of  $37.6 \text{ km s}^{-1}$  in the NH<sub>3</sub> (5.5) line, is shown to be slightly spatially offset from the high-velocity component in Figure 3. We note that, while present, the central velocity of the intermediate-velocity component did vary between the different molecular transitions, ranging from  $\sim 30$ 

**Table 2**Kinematics of the NH<sub>3</sub> (5,5) Transition

Parameter <sup>a</sup>	Value
Low-velocity Component	
$egin{array}{c} v_c \ \sigma \ T_B \end{array}$	$10.6 \pm 2.5 \text{ km s}^{-1}$ $5.8 \pm 2.6 \text{ km s}^{-1}$ $0.01 \pm 0.003 \text{ K}$
Intermediate-velocity Component	
$c$ $\sigma$ $T_B$	$37.6 \pm 5.7 \text{ km s}^{-1}$ $8.0 \pm 3.0 \text{ km s}^{-1}$ $0.05 \pm 0.02 \text{ K}$
High-velocity Component	
$v_c$ $\sigma$ $T_B$	$51.5 \pm 0.6 \text{ km s}^{-1}$ $6.9 \pm 0.3 \text{ km s}^{-1}$ $0.34 \pm 0.03 \text{ K}$

#### Note.

to 45 km s<sup>-1</sup>. Therefore, the error estimates on the central velocity of the intermediate component are much larger than those shown in the low- and high-velocity components to reflect this uncertainty.

We can further analyze the morphology of the molecular emission by isolating the channels associated with each component. Figure 5 shows the distribution of the NH<sub>3</sub> (3,3) emission in each velocity component, labeled by their respective central velocities from Table 2. We are using the NH<sub>3</sub> (3,3) line for this analysis due to the faintness of the low-velocity component in the NH<sub>3</sub> (5,5) transition. When integrating over the field we were sensitive enough to detect the 10.6 km s<sup>-1</sup> component, but for a spatial mapping, the NH<sub>3</sub> (5,5) line is not bright enough to perform a pixel-by-pixel analysis of that component. We are aware that the hyperfine satellite lines of the NH<sub>3</sub> (3,3) emission will be more prominent than in the (5,5) transition and will acknowledge where those lines may contribute in the following discussion.

In general, the observed gas morphology is unique for each velocity component. The 51.5 km s<sup>-1</sup> velocity gas is concentrated toward the center of the field and closely follows the bright NH<sub>3</sub> emission in Figure 2, with the exception of the filamentary extension (e.g., see the wedge-shaped distribution in the red contour; Figure 5). The 10.6 km s<sup>-1</sup> component is distributed throughout the field of view and contains several elongated structures (e.g., black box in Figure 5). Further, this component does not appear to have similar morphology to the 51.5 km s<sup>-1</sup> component, suggesting this gas could be independent of the  $51.5 \text{ km s}^{-1}$  emission. The morphology of the 37.6 km s<sup>-1</sup> component has similar attributes to both the 10.6 and 51.5 km s<sup>-1</sup> components. Unlike the 51.5 km s<sup>-1</sup> component, the 37.6 km s<sup>-1</sup> component is associated with the filamentary extension. Further, the filamentary extension closely follows the elongated structure in the 10.6 km s<sup>-1</sup> component (Figure 5). The 37.6 km s<sup>-1</sup> component also contains concentrated emission toward the north, which spatially overlaps with emission in the 51.5 km s<sup>-1</sup> component. Because of this spatial overlap, some of the 37.6 km s<sup>-1</sup> emission could be from the hyperfine lines in the  $51.5 \text{ km s}^{-1} \text{ component.}$ 

<sup>&</sup>lt;sup>a</sup>  $v_c$  is the central velocity of the component,  $\sigma$  is the velocity dispersion, and  $T_B$  is the peak brightness temperature.

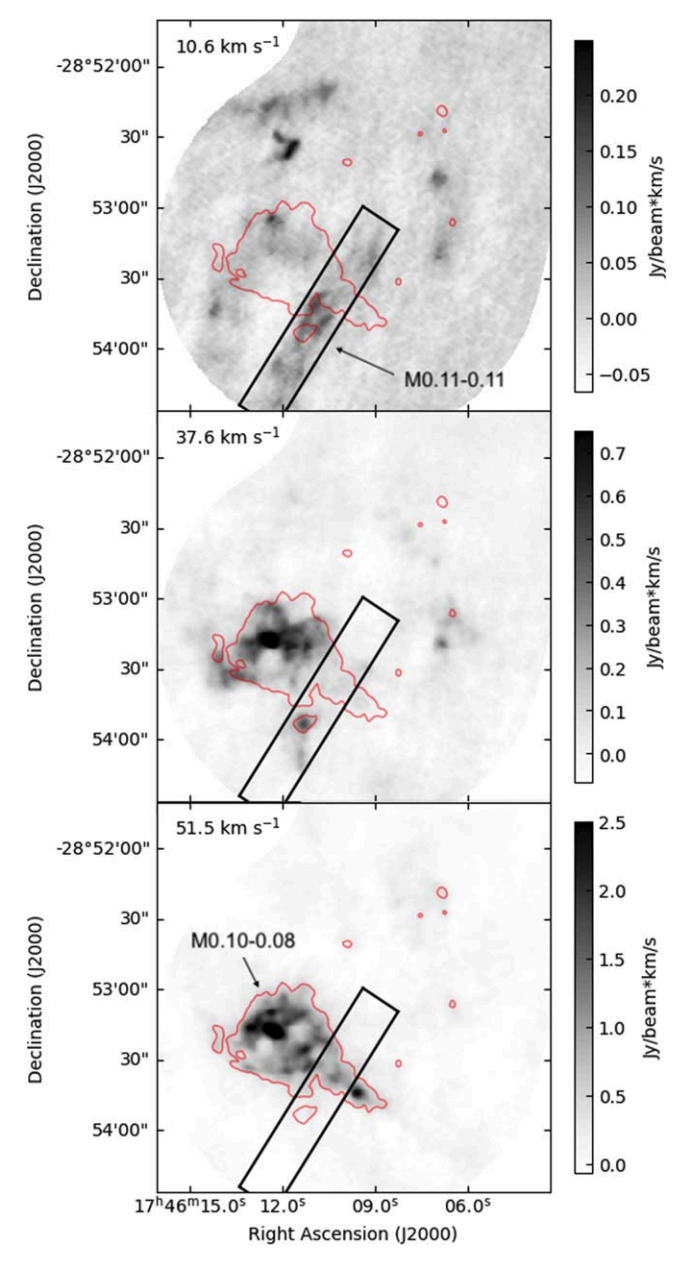


Figure 5. Molecular morphology of the three velocity components presented in Table 2 (integrated intensity, moment 0, in NH<sub>3</sub> (3,3)). These panels were made using  $V_c \pm \sigma_v$  (to the closest channel). The red contour in all three panels shows the  $20\sigma$  level from the "Features" panel in Figure 2 for spatial reference. Annotated on the 10.6 and the 51.5 km s<sup>-1</sup> panels are the M0.11–0.11 and M0.10–0.08 clouds, respectively The black box shows the region used for the position–velocity slice in Figure 7.

#### 3.3. 36.2 GHz CH<sub>3</sub>OH Masers in M0.10-0.08

Our Ka-band observations included the 36.2 GHz CH<sub>3</sub>OH  $(4_{-1}-3_0)$  maser transition. This class I maser is known to trace shocks, as it is collisionally excited (Morimoto et al. 1985; Menten 1991; Sjouwerman et al. 2010). The 36.2 GHz CH<sub>3</sub>OH  $(4_{-1}-3_0)$  maser transition has previously been detected toward this region (Yusef-Zadeh et al. 2013; Cotton & Yusef-Zadeh 2016). Our data suggest there are at least 100 compact CH<sub>3</sub>OH sources in M0.10–0.08 (Figure 2, second row, last panel). The compact CH<sub>3</sub>OH sources in M0.10–0.08 are located within a square arcminute region and closely follow the bulk of the NH<sub>3</sub> and HC<sub>3</sub>N emission at velocities from 40 to 60 km s<sup>-1</sup> (Figure 5, bottom panel).

Figure 6 shows the spatial distribution (left) and the velocity distribution (right) of the bright, above 0.6 Jy beam<sup>-1</sup> ( $12\sigma$ ), 36.2 GHz CH<sub>3</sub>OH emission. The CH<sub>3</sub>OH emission is not uniformly distributed throughout M0.10–0.08. Most of the CH<sub>3</sub>OH emission appears to be distributed throughout the wedge-like structure (discussed in Section 3.1.1). We do not detect any compact emission, above  $12\sigma$ , from the filamentary extension (e.g., see Figures 2 and 6).

The velocity of the  $CH_3OH$  emission in M0.10-0.08 ranges from  $\sim\!35$  to 65 km s<sup>-1</sup>. This corresponds to the velocity range of the bright  $NH_3$  emission (Figure 3). This velocity range indicates that most of the  $CH_3OH$  maser emission is associated with the 37.6 and 51.5 km s<sup>-1</sup> velocity components.

In order to characterize the nature of the point-like emission and to evaluate whether these detections represent maser emission, we used the source detection algorithm Clumpfind (Williams et al. 1994) to distinguish the emission both spectrally and spatially. Clumpfind identifies local maxima and uses saddle points in position and velocity space around the local maxima to determine the boundaries of the sources. Clumpfind then produces a list of clumps with uniform criteria, which was used to construct a catalog (for more details on maser identification using the Clumpfind algorithm, see the description of this technique in Mills et al. 2015, Section 5.1). Sixty-four of the compact CH<sub>3</sub>OH sources have brightness temperatures over 400 K (i.e., "CH<sub>3</sub>OH masers"). The properties of the 64 detected "CH<sub>3</sub>OH masers" identified with Clumpfind are listed in Table A1. The spectral profiles of these masers are shown in Figure A1. The 15 brightest masers in M0.10–0.08 are labeled in Figure 6 (left).

With Clumpfind we also detect 31 compact CH<sub>3</sub>OH sources that have a brightness temperature between 100 and 400 K, which we regard as "maser candidates." These sources are considered to be candidate masers based on their brightness temperatures, which are similar to observed gas temperatures in CMZ clouds (50–400 K, Mills & Morris 2013; Krieger et al. 2017) Therefore, we assume that any emission above this upper 400 K limit is likely nonthermal (i.e., maser emission, sources in Table A1) and any emission that is below 100 K is most likely thermal. Therefore, we classify CH<sub>3</sub>OH point sources that have brightness temperatures between 100 and 400 K as "maser candidates." The properties of all 31 maser candidates are listed in Table A2, with their spectra shown in Figure A2. These maser candidates are also located within the same square arcminute region as the detected CH<sub>3</sub>OH masers and have a similar velocity range  $(41-63 \text{ km s}^{-1})$ .

### 4. Discussion

In the following section, we present a discussion and interpretation of our kinematics results on the M0.10-0.08 cloud (Section 3). Here, we attempt to explain the complicated and multiple-component velocity structure detected in the vicinity of M0.10-0.08 (Sections 4.1 and 4.2).

#### 4.1. Locations and Origins of M0.10-0.08 and M0.11-0.11

The bulk emission in this region of the Galactic center has a velocity of around 51.5 km s<sup>-1</sup> (Section 3.2.1). The morphology and gas kinematics of this velocity component are consistent with those found in previous studies of M0.10–0.08 (e.g., Tsuboi et al. 2011). M0.10–0.08 appears to be part of a larger structure of molecular gas that has a

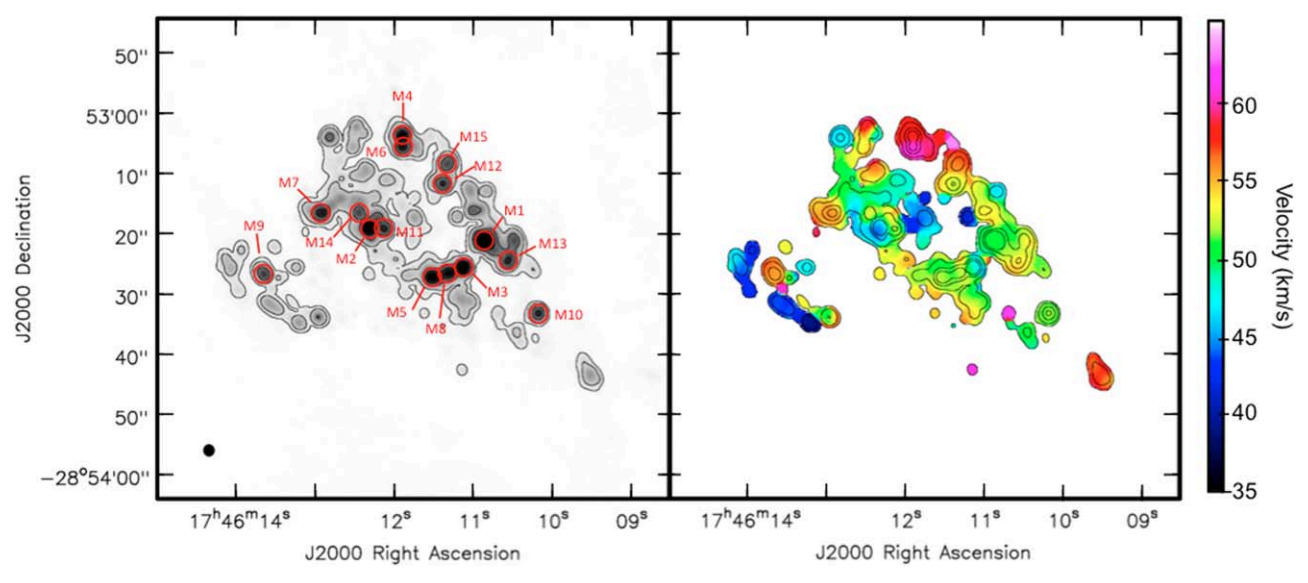


**Figure 6.** Distribution of the 36.2 GHz CH<sub>3</sub>OH  $(4_{-1}-3_0)$  masers in M0.10–0.08 showing the maximum intensity emission (left), from Figure 2, and central velocities (right) for emission above the  $12\sigma$  level. The overlaid contours show 12, 30, 100, and  $200 \times 50$  mJy  $b^{-1}$  (rms noise in the brightest channel). The 15 brightest masers from Table A1 are marked on the left panel.

velocity of around 50 km s<sup>-1</sup> (Fukui et al. 1977; Tsuboi et al. 2011). Tsuboi et al. (2011) detected H<sup>13</sup>CO<sup>+</sup> emission around 50 km s<sup>-1</sup> extending from +0°.15 to -0°.05 ( $d \sim 27$  pc; see their Figure 10). Within this extended diffuse structure, they detect three concentrated regions of H<sup>13</sup>CO<sup>+</sup> emission that coincide with the M0.10–0.08, M0.07–0.07, and 50 km s<sup>-1</sup> (M–0.02–0.07) molecular clouds (see Figure 1 for locations of these clouds). The presence of all three clouds within this larger diffuse structure could be evidence that all three clouds are colocated within a single lower-density envelope that has a velocity of around 50 km s<sup>-1</sup>.

This large diffuse gas structure, observed in H<sup>13</sup>CO<sup>+</sup> by Tsuboi et al. (2011), may be Orbital Stream 1 in the Kruijssen et al. (2015) orbital model. The  $50 \text{ km s}^{-1}$  cloud is argued to be associated with Orbital Stream 1 (Kruijssen et al. 2015). Therefore, if M0.10-0.08 and M-0.02-0.07 are associated within the same gas stream and the 50 km s<sup>-1</sup> cloud is located on Orbital Stream 1, then by extension we can infer that M0.10-0.08 is also located on Orbital Stream 1. We note, however, that in the Kruijssen et al. (2015) orbital stream model, gas at the closest angular location to the M0.10 -0.08 cloud (1 = 0.09, b = -0.07; as the position of M0.10 -0.08 is slightly offset from Orbital Stream 1 by  $\sim 1'$ ) is predicted to have a line-of-sight velocity of 60 to 65 km s<sup>-1</sup>. Although this suggested line-of-sight velocity is slightly higher than the central velocity of M0.10-0.08 that we measured in Figure 4, we do detect some gas at velocities of around 60 to 65 km  $s^{-1}$  (see Figures 3 and 6, right).

The M0.20–0.033 expanding shell is also hypothesized to be located on Orbital Stream 1 (Butterfield et al. 2018; see our Figure 1 for the spatial location of the shell relative to other GC clouds). In Butterfield et al. (2018) we reported a systemic velocity of  $\sim\!53~\rm km~s^{-1}$  for the M0.20–0.033 expanding shell and advocate that the shell is also located on Orbital Stream 1, based on a position–velocity analysis. Indeed, the adjacent locations of M0.10–0.08 and the M0.20–0.033 expanding shell (see Figure 1) and their similar velocities are consistent with both clouds being on the same orbital stream. Additionally, based on the orbital direction of stream 1, the M0.10–0.08 cloud

would be located "upstream" from the M0.20–0.033 expanding shell. Based on the orbital solution in Kruijssen et al. (2015), M0.10–0.08 would orbit into the current location of the M0.20–0.033 expanding shell in  $\sim$ 0.05 Myr.

The 10.6 km s<sup>-1</sup> component (Figure 4; Section 3.2) covers a velocity range of  $\sim 0-20 \text{ km s}^{-1}$  based on analysis of the NH<sub>3</sub> (5,5) emission and additional analysis of the HC<sub>3</sub>N lines. This velocity range is similar to observed velocities of the adjacent M0.11–0.11 molecular cloud ( $\sim$ 10–30 km s<sup>-1</sup>; Jones et al. 2012; Clavel et al. 2013, see their Figure 2) and nearby gas velocities associated with Kruijssen et al.'s (2015) orbital stream 3 ( $\sim$ 0–5 km s<sup>-1</sup>). However, there are discrepancies in the literature concerning the velocity of the M0.11-0.11 cloud. Tsuboi et al. (1997), Handa et al. (2006), and Tsuboi et al. (2011) report a slightly higher velocity range of 15–45 km s<sup>-1</sup>. These velocity values of the M0.11–0.11 cloud in Tsuboi et al. (1997), Handa et al. (2006), and Tsuboi et al. (2011) are closer to those of the intermediate-velocity component in our observations (37.6 km s<sup>-1</sup>; see Section 3.2.1). In our Figure 4, this velocity component appears as a lower-velocity "wing" of the main 51.5 km s<sup>-1</sup> component, rather than a distinct cloud. Further, the morphology of the 37.6 km s<sup>-1</sup> component in Figure 5 appears to overlap with the  $51.5 \text{ km s}^{-1}$  component with the exception of the filamentary extension. Therefore, based on the previous work of Jones et al. (2012) and Clavel et al. (2013) and our analysis above, we interpret the 10.6 km s<sup>-1</sup> component as extended emission associated with M0.11-0.11.

### 4.1.1. Similar X-Ray Fluorescence Detected in Both M0.10 –0.08 and M0.11 –0.11

Observed X-ray fluorescence can be beneficial in determining radial distances, which, when combined with their projected separation from the Galactic center, can be used to infer intercloud distances (e.g., Clavel et al. 2013; Terrier et al. 2018). In our Galactic center, fluorescent iron emission at 6.4 keV is created in molecular clouds by K-shell photoionization and Compton scattering of neutral iron atoms from a previous, gigantic X-ray flare, presumably from Sgr A\*. By observing the time delay of the detected X-ray reflection across

multiple molecular clouds, we can constrain the locations of clouds from the geometrical path length between the clouds and Sgr and determine their location along our line of sight (e.g., Cramphorn & Sunyaev 2002). Further, the time delay between the detected reflections provides a measurement of the total path traveled by the photons, assuming they were emitted simultaneously. This path length then gives an indication of the relative locations of the clouds.

Molecular clouds that show similar illumination at a similar timeframe are located along the same three-dimensional "parabola," assuming the illumination feature is produced by the same, single flaring event (e.g., Sunyaev & Churazov 1998). Along this three-dimensional parabola, the path length of the propagating light signal (from Sgr A\* to the cloud and then to Earth) is the same at each location, and therefore, the time delay of the propagating signal is the same as well. Clavel et al. (2013) detected a similar X-ray fluorescence signature in both M0.10-0.08 and M0.11-0.11 (sources Br2 and G0.11-011 in their study). 14 This detection of similar X-ray fluorescence illumination in M0.10-0.08 and M0.11-0.11 indicates the two clouds are located along the same three-dimensional parabola, assuming the fluorescence in both clouds is from the same event. Further, because the two clouds are aligned along the same line of sight and have a similar X-ray fluorescence light curve, Clavel et al. (2013) argue the two clouds must be at the same physical position, even with their differences in velocity. If the two clouds are almost at the same physical location, then we would expect to see evidence of this interaction.

### 4.2. Proposed Physical Interaction between M0.10–0.08 and M0.11–0.11

Previous studies have hinted at a possible connection between M0.10–0.08 and M0.11–0.11 (Handa et al. 2006; Clavel et al. 2013). However, because of the large velocity difference between the two clouds along this line of sight  $(\Delta v \sim 30~{\rm km~s^{-1}})$ , other investigators have suggested these components are physically separated (Ponti et al. 2010; Kruijssen et al. 2015). The high-resolution data presented in this paper can provide insight into this discrepancy in the literature. In this section, we perform a detailed position–velocity analysis on this region to investigate a possible connection between M0.10–0.08 and M0.11–0.11.

Figure 7 shows the position–velocity distribution of  $NH_3(3,3)$  (top) and  $HC_3N(3-2)$  (bottom) across the filamentary extension (black box in Figure 5). This slice was selected to maximize the relatively faint signal of the M0.11-0.11 cloud (top panel in Figure 5) and illustrate a possible connection to M0.10-0.08. The slice contains emission in all three velocity components (Table 2 and Figure 5). Emission associated with the M0.10-0.08 cloud is clearly the brightest component in this region ( $50-60 \text{ km s}^{-1}$ ), with possible hyperfine lines above and below the main emission region (blue shaded region in Figure 7, top). These hyperfine lines have a fixed known separation from the main component of  $\pm 21.1 \text{ km s}^{-1}$  and  $\pm 29.1 \text{ km s}^{-1}$  for the  $NH_3$  (3,3) transition (e.g., Krieger et al. 2017). The  $NH_3$  emission at  $\sim 80 \text{ km s}^{-1}$  is not observed in  $HC_3N$  (3–2) (Figure 7, bottom), suggesting it is hyperfine line emission. Across this slice, there is a clear,

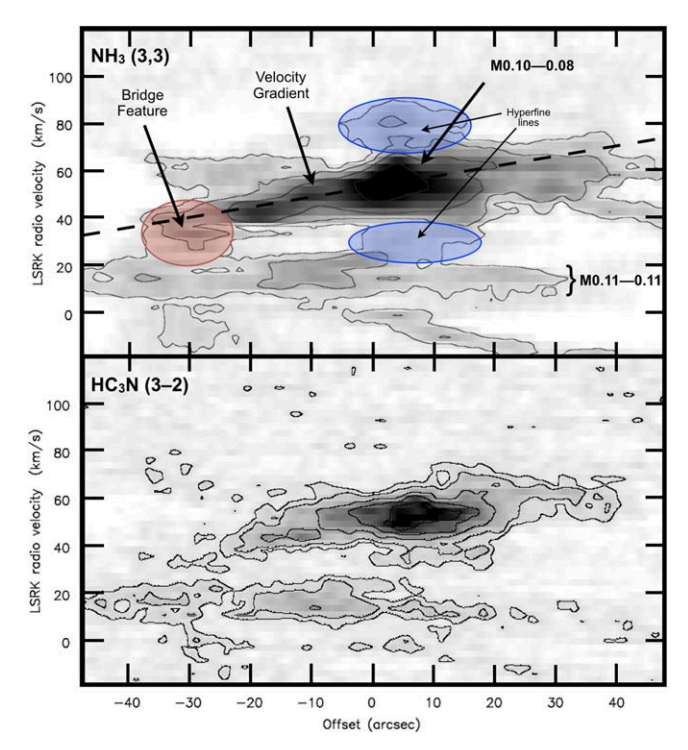


**Figure 7.** Position–velocity distribution across the spatial slice shown in Figure 5, for NH<sub>3</sub> (3,3) (top) and HC<sub>3</sub>N (3–2) (bottom). Annotations in the top panel show the gas associated with M0.11–0.11 and M0.10–0.08 (see Section 4.1). The black dashed line shows the magnitude and orientation of the  $\sim$ 10 km s<sup>-1</sup> pc<sup>-1</sup> velocity gradient described in Section 3.2. The blue regions in the top panel show the general locations of the hyperfine satellite lines ( $\pm$ 20–30 km s<sup>-1</sup> from the main component) of M0.10–0.08. The red shaded region highlights the "bridge"-like feature discussed in Section 4.2.

extended emission in M0.11-0.11 (10.6 km s<sup>-1</sup> component; Figure 7, top). The emission in M0.11-0.11 is relatively faint compared to M0.10-0.08 and spans a velocity range from 5 to 25 km s<sup>-1</sup>.

The 37.6 km s<sup>-1</sup> component appears as a lower-velocity wing to the  $51.5 \text{ km} \text{ s}^{-1}$  component in the integrated spectrum (Figure 4). When isolating velocity channels associated with each component, we see that some of the gas in the 37.6 km s<sup>-1</sup> component is spatially offset from the 51.5 km s<sup>-1</sup> component (Figure 5). We also observe this offset in position-velocity space, where some of the gas in the 37.6 km s<sup>-1</sup> component appears to be spatially offset from the bulk of the 51.5 km s<sup>-1</sup> component (Figure 7, top). Additionally, the 37.6 km s<sup>-1</sup> component is mainly associated with emission along the velocity gradient (see Section 3.2) and appears to be a distinct feature in position-velocity space. Further, at the southern edge of the velocity gradient, there is a bridge feature with emission between velocities 20 and 40 km s<sup>-1</sup> (red shaded region in Figure 7, top). Including both the bridge feature and the velocity gradient results in continuous emission between 20 and 50 km s<sup>-1</sup>, thereby showing that M0.10-0.08 and M0.11-0.11 have an apparent connection in position-velocity space. Analysis of the HC<sub>3</sub>N (3-2) line shows a similar velocity gradient and bridge-like features across the slice (Figure 7, bottom). However, the HC<sub>3</sub>N emission is  $\sim$ 5×-10× fainter than the NH<sub>3</sub>(3,3) line, so these features appear loosely connected and barely above the noise level.

Recent studies simulating Galactic cloud-cloud interactions predict a broad "bridge"-like feature in position-velocity space,

<sup>&</sup>lt;sup>14</sup> The data presented in Clavel et al. (2013) used Chandra observations from 1999 to 2011 (see their Table 1 for observational information). These X-ray observations had a resolution of 4" and are therefore fairly comparable to the observations presented in this paper, Table 1.

where the two clouds are physically connected (e.g., Takahira et al. 2014; Haworth et al. 2015; Torii et al. 2017). <sup>15</sup> In these studies, there is intermediate-velocity gas between the two main cloud components, which produces the "bridge" in position–velocity space. Such bridge features have since been detected in numerous molecular clouds throughout the galaxy (e.g., Fukui et al. 2016; Torii et al. 2017).

Large-scale observations ( $\sim 45''$  resolution) of the intermediate-velocity component (15–45 km s<sup>-1</sup>) from Tsuboi et al. (1997) and Handa et al. (2006) show the gas is extended and dense. Tsuboi et al. (1997) extracted a position-velocity slice at b = -6' ( $4' \le l \le 14'$ ) from their CS data cubes and observed two vertical features in velocity space that spanned 15 km s<sup>-1</sup> to 40 km s<sup>-1</sup> and were separated by  $\sim$ 2' (see their Figure 2). Handa et al. (2006) also saw similar vertical features in velocity space in their H<sup>13</sup>CO<sup>+</sup> and SiO data cubes. Tsuboi et al. (1997) attribute the vertical velocity features to an expanding shell centered on a lower emission region near the centroid of the cloud, where the bright vertical features are the limb-brightened edges of the shell. However, these vertical features could alternatively be signatures of the bridge feature, discussed above, on larger scales. At the low spatial resolution of the Handa et al. (2006) and Tsuboi et al. (1997) observations  $(\sim 45'')$ , the detailed substructure we observed at -45'' to 0'' in Figure 7 (top) would blend into a single pixel. Therefore, the high-resolution gradient and bridge features shown in Figure 7 would appear as broad, continuous emission at 45" resolution.

Thus, based on the close physical proximity of M0.10–0.08 and M0.11–0.11 from X-ray fluorescence data, along with continuous emission connecting them in position–velocity space via a "bridge" feature, we argue the two clouds are physically interacting. Furthermore, this would imply that M0.11–0.11 is located on the same stream as M0.10–0.08 and not on a separate stream as indicated by the Kruijssen et al. (2015) orbital model.

#### 4.3. Gas Kinematics in the CMZ Clouds

Disentangling the molecular gas kinematics in CMZ clouds can be complex. As we have shown in this paper, the multiple velocity components toward the M0.10–0.08 cloud can make isolating the individual components challenging. For example, extensive efforts were conducted to fit the three components, with similar Gaussian fit parameters ( $V_c$  and  $\sigma$ ), across multiple NH<sub>3</sub> transitions. However, we were unable to get converging values that satisfied the multiple transitions. The lower J transitions had a brighter hyperfine structure for each component resulting in over nine blended profiles within the  $\sim 0-70~{\rm km~s}^{-1}$  velocity range, which could be fit with numerous solutions. At the higher J transitions, the 10.6 km s<sup>-1</sup> component was not bright enough to fit the spectrum.

s<sup>-1</sup> component was not bright enough to fit the spectrum. The 37.6 km s<sup>-1</sup> component was also especially challenging to fit. Because this component appears as a low-velocity wing to the 51.5 km s<sup>-1</sup> component, there were numerous solutions to the profile that varied depending on the initial guesses and range limits in the pyspeckit program, with central velocity values that ranged from  $\sim$ 30 to 45 km s<sup>-1</sup>. However, the presence of an intermediate-velocity component between  $\sim$ 30 and 45 km s<sup>-1</sup> was clear in all of our NH<sub>3</sub> and HC<sub>3</sub>N transitions

(illustrated by the dashed green residuals in Figure 4). The fit solution we present in this paper (see Table 2) was the best-fit parameters that accurately reflected the uncertainty in the 37.6 km s<sup>-1</sup> component. However, we note that determining a simple kinematic solution to complex kinematics in the CMZ can be problematic and requires multiple methods to disentangle the velocity components (i.e., spectral fitting, position–velocity analysis, moment images of components, etc.).

Furthermore, the complex kinematics in the CMZ can make understanding the gas flows and unusual orbits more challenging. We have attempted to disentangle the kinematics toward this complicated region using high-spatial- and high-spectralresolution observations. While we were able to identify the three velocity components toward this region using a variety of methods, providing a simple solution that satisfies the kinematics observed in this data set is more difficult. Future observations of complex kinematic regions should use a variety of methods to isolate the velocity components. If possible, future observations should also use absorption observations toward radio continuum regions to constrain the line-of-sight arrangement, similar to the approach we used in Butterfield et al. (2018). Despite the complexity of disentangling the kinematics of multiple components, the analysis is necessary to constrain models of the large-scale gas structures. Models for the three-dimensional orientations of these gas structures can be influenced by assumptions made in complex kinematic regions. Therefore, applying the solutions in complex kinematic regions in the models may help resolve some of the contingencies in future orbital solutions.

#### 5. Summary

We present high-resolution ( $\sim$ 3") VLA radio observations of the compact (3 pc) M0.10–0.08 molecular cloud, finding that it is composed of multiple compact molecular clumps (5+clumps;  $D_{\rm clumps} \leq 0.4$  pc; Section 3.1). We detect 15 molecular transitions in M0.10–0.08 (Table 1), including 8 transitions of NH<sub>3</sub>, 2 HC<sub>3</sub>N transitions, OCS, CH<sub>3</sub>CN, HC<sub>5</sub>N, and abundant 36.2 GHz CH<sub>3</sub>OH masers (see Section 3.3 and the Appendix for details on the detected masers).

The main focus of this paper is on the molecular gas kinematics toward M0.10-0.08. We present the following results from this study:

(1) Three velocity components detected toward M0.10-0.08: The averaged NH<sub>3</sub> (5,5) spectrum reveals three velocity components centered at 10.6, 37.6, and 51.5 km s<sup>-1</sup> (see Section 3.2.1, Figures 4 and 5, and Table 2). Initially, the NH<sub>3</sub> (5,5) spectrum was fit with two Gaussian components at  $\sim 10-15$  km s<sup>-1</sup> and  $\sim 50-55$  km s<sup>-1</sup>. However, the residuals of this fit showed excess emission around 20-40 km s<sup>-1</sup>, which we interpreted to be a third velocity component (see green dashed line in Figure 4) In our high-resolution data, the 51.5 km s<sup>-1</sup> component is the brightest emission in this region. The 10.6 km s<sup>-1</sup> component is relatively faint compared to the other two components in the field. We have also analyzed the gas morphology in each component by isolating channels associated with each component (Figure 5). The morphology in all three components is unique.

(2) Relationship between M0.10-0.08 and Orbital Stream 1: M0.10-0.08 is part of a larger structure of gas that contains the M-0.02-0.07 and M0.07-0.07 molecular clouds and has a velocity of around 50 km s<sup>-1</sup> (Tsuboi et al. 2011). The central velocity of M0.10-0.08 (51.5 km s<sup>-1</sup>; Section 4.1) indicates

 $<sup>\</sup>overline{^{15}}$  This labeling of the "bridge"-like feature in position-velocity space, defined in Haworth et al. (2015), should not be confused with the X-ray definition of the Bridge, labeled as Br1 and Br2 (Ponti et al. 2010; Clavel et al. 2013), which spatially connects M-0.02-0.07 to M0.10-0.08.

that M0.10-0.08 is likely located on Orbital Stream 1 in the Kruijssen et al. (2015) model.

(3) Resolving the kinematics of M0.11-0.11: Discrepant reports regarding the central velocity of M0.11-0.11 range from 10 to 45 km s<sup>-1</sup>. In our high-resolution data, we detect two components in this velocity range: 10.6 and 37.6 km s<sup>-1</sup>. We argue that gas in the 10.6 km s<sup>-1</sup> component is associated with M0.11-0.11 as the morphology is distinct from that of the M0.10-0.08 cloud (Figure 5). Additionally, a position-velocity analysis toward this region of the CMZ shows extended emission (>70"; >2.7 pc) from 0 to 20 km s<sup>-1</sup> (Figure 7), which we suggest is associated with M0.11-0.11.

(4) Physical interaction between M0.10–0.08 and M0.11–0.11: Past X-ray fluorescence observations by Clavel et al. (2013) show similar time-delay signatures from both M0.10–0.08 and M0.11–0.11 and argue the two clouds are in the same physical position of the Galactic center. The intermediate morphology of the 37.6 km s<sup>-1</sup> velocity component could be indicative of physical interaction between M0.10–0.08 and M0.11–0.11. Indeed, all three velocity components appear to be connected in position–velocity space (Figure 7). The intermediate-velocity component, which has similar features to both M0.10–0.08 and M0.11–0.11, could be gas from where these two are physically connected.

This material is based upon work supported by grants from the National Science Foundation (NSF; Nos. AST-0907934, AST-15243000, AST-1614782, AST-2008101, CAREER-2142300). Support for this work was also provided by the NSF through the Grote Reber Fellowship Program administered by Associated Universities, Inc./National Radio Astronomy Observatory.

N.O.B. would like to thank Dr. Farhad Yusef-Zadah (Northwestern University), Dr. Robert Mutel (University of Iowa), Dr. Steven Spangler (University of Iowa), and Dr. Kennith Gayley (University of Iowa) for their helpful critique on this thesis analysis. The authors would also like to thank Dr. Allison Costa (University of Virginia), Dr. Monica Sanchez (University of New Mexico), and Dr. Diederik Kruijssen (Max-Planck Institute) for their helpful insight on this work.

The authors would like to thank Dr. Elisabeth Mills (University of Kansas) for her helpful insight on the spectral line fitting and analysis of the results presented in this paper. The authors would also like to thank Dr. John Bally for his inspiration in creating the 3-color image shown in Figure 1. The authors would like to thank the anonymous referee for their helpful insight into this manuscript.

*Software:* CASA (International Consortium Of Scientists 2011); Clumpfind (Williams et al. 2011); pyspeckit (Ginsburg & Mirocha 2011; Ginsburg et al. 2022).

## Appendix Catalog of CH<sub>3</sub>OH Masers in M0.10-0.08

To catalog the properties of these masers, we used the Clumpfind algorithm (Williams et al. 1994). We define all compact sources with peak brightness temperatures above  $400~\rm K$  as  $\rm CH_3OH$  masers in this paper, following the classification used in Mills et al. (2015). Table A1 presents the properties of these 64 masers, with their spectra shown in Figure A1. Table A2 lists the maser candidates with their spectra shown in Figure A2. Results of all 95 detected compact  $\rm CH_3OH$  sources (both masers and candidate masers) are discussed in Section 3.3.

**Table A1**36.2 GHz CH<sub>3</sub>OH Masers in M0.10–0.08

ID	Maser Name	α (J2000)	δ (J2000)	$\frac{v}{\text{km s}^{-1}}$	FWHM km s <sup>-1</sup>	I <sub>peak</sub> Jy b <sup>-1</sup>	Flux Jy km s <sup>-1</sup>	T <sub>b</sub>	Resolved?
3.61	350 1020 (14 0 0002 (24								
M1	M0.1039644-0.0802624	17 <sup>h</sup> 46 <sup>m</sup> 10 <sup>s</sup> 85	-28°53′21″1	50.60	3.911	46.969	265.944	12438	YES
M2	M0.1072762-0.0845517	17 <sup>h</sup> 46 <sup>m</sup> 12 <sup>s</sup> 33	-28°53′18″9	43.25	7.833	29.621	252.342	7844	YES
M3	M0.1033757-0.0817884	17 <sup>h</sup> 46 <sup>m</sup> 11 <sup>s</sup> 12	-28°53′25″7	46.40	4.332	24.917	100.982	6598	NO
M4	M0.1100239-0.0810107	17 <sup>h</sup> 46 <sup>m</sup> 11.89	-28°53′03″8	59.00	3.289	20.721	89.420	5487	YES
M5	M0.1038130-0.0832737	17 <sup>h</sup> 46 <sup>m</sup> 11.53	-28°53′27″2	52.70	4.527	19.008	131.418	5033	YES
M6	M0.1096832-0.0812181	17 <sup>h</sup> 46 <sup>m</sup> 11 <sup>s</sup> 89	-28°53′05″3	61.10	3.197	16.980	70.044	4496	YES
M7	M0.1090134-0.0860631	17 <sup>h</sup> 46 <sup>m</sup> 12 <sup>s</sup> .93	-28°53′16″4	55.85	4.772	16.369	141.360	4334	YES
M8	M0.1035684-0.0824885	17 <sup>h</sup> 46 <sup>m</sup> 11 <sup>s</sup> 32	-28°53′26″4	51.65	4.394	15.666	108.233	4148	YES
M9	M0.1078915-0.0897819	17 <sup>h</sup> 46 <sup>m</sup> 13 <sup>s</sup> 64	-28°53′26″8	54.80	2.835	15.543	62.866	4116	NO
M10	M0.0997717-0.0798958	17 <sup>h</sup> 46 <sup>m</sup> 10 <sup>s</sup> 17	-28°53′33″3	50.60	2.093	13.577	41.198	3595	NO
M11	M0.1068280-0.0840072	17 <sup>h</sup> 46 <sup>m</sup> 12 <sup>s</sup> 14	-28°53′19″3	51.65	6.166	11.870	133.134	3143	YES
M12	M0.1072164-0.0806180	17 <sup>h</sup> 46 <sup>m</sup> 11 <sup>s</sup> .40	-28°53′11″7	51.65	4.871	11.623	82.500	3078	YES
M13	M0.1026273-0.0797920	17 <sup>h</sup> 46 <sup>m</sup> 10 <sup>s</sup> .55	-28°53′24″3	54.80	5.653	11.497	121.184	3044	YES
M14	M0.1081318-0.0846147	17 <sup>h</sup> 46 <sup>m</sup> 12 <sup>s</sup> 46	-28°53′16.″4	55.85	5.166	10.121	82.795	2680	YES
M15	M0.1078793-0.0799809	17 <sup>h</sup> 46 <sup>m</sup> 11 <sup>s</sup> 34	-28°53′08″5	55.85	4.417	10.026	70.744	2655	YES
M16	M0.1117873-0.0839075	17 <sup>h</sup> 46 <sup>m</sup> 12 <sup>s</sup> . 82	-28°53′03″8	46.40	3.953	9.862	48.569	2611	NO
M17	M0.1032901-0.0791549	17 <sup>h</sup> 46 <sup>m</sup> 10 <sup>s</sup> . 50	-28°53′21″1	52.70	5.703	9.169	86.949	2428	YES
M18	M0.1054681-0.0800475	17 <sup>h</sup> 46 <sup>m</sup> 11 <sup>s</sup> .02	-28°53′16″0	52.70	6.421	7.465	55.618	1977	YES
M19	M0.1048914-0.0886890	17 <sup>h</sup> 46 <sup>m</sup> 12 <sup>s</sup> . 96	$-28^{\circ}53'34\rlap.{''}0$	55.85	3.140	6.689	23.222	1771	NO
M20	M0.0961419-0.0793034	17 <sup>h</sup> 46 <sup>m</sup> 09 <sup>s</sup> .51	-28°53′43″3	57.95	9.415	6.398	75.184	1694	YES
M21	M0.1090096-0.0854816	17 <sup>h</sup> 46 <sup>m</sup> 12 <sup>s</sup> .79	-28°53′15″3	50.60	7.226	5.984	61.843	1584	YES
M22	M0.1089767-0.0909895	17 <sup>h</sup> 46 <sup>m</sup> 14 <sup>s</sup> 08	-28°53′25″7	44.30	4.955	5.751	51.748	1522	YES
M23	M0.1090577-0.0849852	17 <sup>h</sup> 46 <sup>m</sup> 12 <sup>s</sup> 68	-28°53′14″2	49.55	6.802	5.465	58.627	1447	YES
M24	M0.1115057-0.0826777	17 <sup>h</sup> 46 <sup>m</sup> 12 <sup>s</sup> 49	-28°53′02."4	60.05	2.935	5.460	22.068	1445	NO
M25	M0.1066804-0.0902855	17 <sup>h</sup> 46 <sup>m</sup> 13 <sup>s</sup> 59	-28°53′31″5	44.30	4.414	5.459	40.981	1445	YES
M26	M0.1034462-0.0820959	17 <sup>h</sup> 46 <sup>m</sup> 11.21	-28°53′26″1	59.00	5.071	5.279	38.491	1398	YES

Table A1 (Continued)

ID	Maser Name	α (J2000)	δ (J2000)	$v \ { m km \ s}^{-1}$	FWHM km s <sup>-1</sup>		Flux Jy km s <sup>-1</sup>	$T_b$ K	Resolved?
M27	M0.1084206-0.0843221	17 <sup>h</sup> 46 <sup>m</sup> 12 <sup>s</sup> 44	-28°53′15″0	48.50	6.924	5.277	77.437	1397	YES
M28	M0.1051877-0.0895595	17 <sup>h</sup> 46 <sup>m</sup> 13 <sup>s</sup> 20	-28°53′34″7	39.05	2.862	5.217	18.355	1381	YES
M29	M0.1101091–0.0809589	17 <sup>h</sup> 46 <sup>m</sup> 11 § 89	-28°53′03″5	54.80	3.356	5.175	31.380	1370	YES
M30	M0.1062866-0.0796660	17 <sup>h</sup> 46 <sup>m</sup> 11 <sup>s</sup> 04	-28°53′12″8	52.70	5.321	4.661	36.543	1234	YES
M31	M0.0958678-0.0792367	17 <sup>h</sup> 46 <sup>m</sup> 09 <sup>s</sup> 46	-28°53′44″0	53.75	3.893	4.447	20.439	1177	NO
M32	M0.1096798-0.0833221	17 <sup>h</sup> 46 <sup>m</sup> 12 <sup>s</sup> 38	-28°53′09″2	59.00	3.828	4.372	26.852	1157	NO
M33	M0.1107909-0.0832296	17 <sup>h</sup> 46 <sup>m</sup> 12 <sup>s</sup> 52	-28°53′05″6	54.80	4.924	4.322	29.242	1144	NO
M34	M0.1095427-0.0832887	17h46m12 s 36	-28°53′09″6	52.70	4.907	4.176	46.350	1105	YES
M35	M0.1064915-0.0901670	17 <sup>h</sup> 46 <sup>m</sup> 13 <sup>s</sup> 53	-28°53′31″8	41.15	6.140	4.170	35.602	1104	YES
M36	M0.1022351-0.0825996	17 <sup>h</sup> 46 <sup>m</sup> 11 <sup>s</sup> 15	-28°53′30″8	52.70	5.473	3.974	49.319	1052	YES
M37	M0.1065278-0.0825552	17 <sup>h</sup> 46 <sup>m</sup> 11 <sup>s</sup> 75	-28°53′17″5	44.30	6.437	3.715	33.159	983	YES
M38	M0.1019943-0.0823959	$17^{h}46^{m}11 \stackrel{s}{.} 07$	-28°53′31″1	50.60	4.645	3.549	28.575	939	YES
M39	M0.1093989-0.0901487	17 <sup>h</sup> 46 <sup>m</sup> 13 <sup>s</sup> 94	-28°53′22″9	42.20	4.945	3.496	25.923	925	YES
M40	M0.1111797-0.0825258	17 <sup>h</sup> 46 <sup>m</sup> 12 <sup>s</sup> 41	-28°53′03″1	43.25	3.953	3.494	12.724	925	NO
M41	M0.1114205-0.0827295	17 <sup>h</sup> 46 <sup>m</sup> 12 <sup>s</sup> 49	-28°53′02″8	55.85	4.550	3.452	32.194	914	NO
M42	M0.1058716-0.0789844	17 <sup>h</sup> 46 <sup>m</sup> 10 <sup>s</sup> 82	-28°53′12″8	46.40	4.554	3.103	19.923	821	YES
M43	M0.1074210-0.0884336	17h46m13 s 26	-28°53′25″7	47.45	1.695	3.022	7.059	800	NO
M44	M0.1055756-0.0807994	17 <sup>h</sup> 46 <sup>m</sup> 11 <sup>s</sup> 21	-28°53′17″1	41.15	3.012	2.965	9.531	785	YES
M45	M0.1087352-0.0827294	17 <sup>h</sup> 46 <sup>m</sup> 12 <sup>s</sup> 11	-28°53′11″0	48.50	3.934	2.695	26.288	713	YES
M46	M0.1074951-0.0893226	17 <sup>h</sup> 46 <sup>m</sup> 13 <sup>s</sup> 48	-28°53′27″2	50.60	2.287	2.534	5.071	671	NO
M47	M0.1083131-0.0835702	17 <sup>h</sup> 46 <sup>m</sup> 12 <sup>s</sup> 25	-28°53′13″9	48.50	8.930	2.459	32.152	651	YES
M48	M0.1044687-0.0841590	17 <sup>h</sup> 46 <sup>m</sup> 11 <sup>s</sup> 84	-28°53′26″8	51.65	4.615	2.431	20.260	643	YES
M49	M0.1050284-0.0887224	17 <sup>h</sup> 46 <sup>m</sup> 12 <sup>s</sup> 98	-28°53′33″6	46.40	7.745	2.388	27.822	632	YES
M50	M0.1079693-0.0912524	17 <sup>h</sup> 46 <sup>m</sup> 14 <sup>s</sup> 00	-28°53′29″3	42.20	4.190	2.353	22.536	623	YES
M51	M0.1090804-0.0911599	17 <sup>h</sup> 46 <sup>m</sup> 14 <sup>s</sup> 13	-28°53′25″7	40.10	3.113	2.304	11.128	610	NO
M52	M0.0995238-0.0812144	17 <sup>h</sup> 46 <sup>m</sup> 10 <sup>s</sup> .44	-28°53′36″5	50.60	3.536	2.292	16.356	606	YES
M53	M0.1026091-0.0822551	17 <sup>h</sup> 46 <sup>m</sup> 11 <sup>s</sup> 12	-28°53′29″0	45.35	4.354	2.184	13.540	578	NO
M54	M0.1087914-0.0887671	17 <sup>h</sup> 46 <sup>m</sup> 13 <sup>s</sup> 53	-28°53′22″1	52.70	1.771	2.105	4.209	557	NO
M55	M0.1099096-0.0844667	17 <sup>h</sup> 46 <sup>m</sup> 12 <sup>s</sup> 68	-28°53′10″7	48.50	5.256	2.009	26.867	531	YES
M56	M0.1071396-0.0898893	17 <sup>h</sup> 46 <sup>m</sup> 13 <sup>s</sup> 56	-28°53′29″3	60.05	2.557	1.847	5.353	489	NO
M57	M0.1055655-0.0897965	17 <sup>h</sup> 46 <sup>m</sup> 13 <sup>s</sup> 31	-28°53′34″0	42.20	6.025	1.838	18.726	486	YES
M58	M0.1105910-0.0840519	17 <sup>h</sup> 46 <sup>m</sup> 12 <sup>s</sup> 68	-28°53′07″8	52.70	4.022	1.737	18.043	460	YES
M59	M0.1017160-0.0790623	17h46m10 s 25	-28°53′25″7	51.65	2.259	1.690	9.070	447	YES
M60	M0.1061836-0.0848665	17h46m12:25	-28°53′22″9	53.75	4.861	1.662	13.114	440	NO
M61	M0.1053243-0.0842220	17 <sup>h</sup> 46 <sup>m</sup> 11 <sup>s</sup> 97	-28°53′24″3	54.80	3.553	1.640	11.119	434	YES
M62	M0.1007572-0.0815144	17 <sup>h</sup> 46 <sup>m</sup> 10 <sup>s</sup> .69	-28°53′33″3	62.15	2.780	1.592	5.730	421	NO
M63	M0.1094015-0.0799883	17 <sup>h</sup> 46 <sup>m</sup> 11 <sup>s</sup> 56	-28°53′03″8	56.90	7.673	1.539	17.278	407	YES
M64	M0.0068760-0.0835109	17h46m12 s 03	-28°53′18″2	43.25	6.249	1.538	26.383	407	YES

ID	Maser Name	$\alpha$	δ	ν	FWHM	$I_{\mathrm{peak}}$	Flux	$T_b$	Resolved?
		(J2000)	(J2000)	$\mathrm{km}~\mathrm{s}^{-1}$	$km s^{-1}$	$Jy b^{-1}$	Jy km s <sup>-1</sup>	K	
CM1	M0.1017240-0.0829108	17 <sup>h</sup> 46 <sup>m</sup> 11 <sup>s</sup> 15	-28°53′32″9	55.85	6.634	1.498	20.043	396	YES
CM2	M0.1073500-0.0827553	17 <sup>h</sup> 46 <sup>m</sup> 11 <sup>s</sup> 92	-28°53′15″3	45.35	6.884	1.436	17.249	380	YES
CM3	M0.1087496-0.0796846	17 <sup>h</sup> 46 <sup>m</sup> 11 <sup>s</sup> 40	-28°53′05″3	63.20	6.767	1.418	17.226	375	YES
CM4	M0.1057278-0.0831589	17 <sup>h</sup> 46 <sup>m</sup> 11 <sup>s</sup> .78	-28°53′21″1	48.50	8.387	1.366	14.389	361	YES
CM5	M0.1114133-0.0842520	17 <sup>h</sup> 46 <sup>m</sup> 12 <sup>s</sup> 85	-28°53′05″6	50.60	3.705	1.365	8.593	361	YES
CM6	M0.0994242-0.0843109	17 <sup>h</sup> 46 <sup>m</sup> 11 <sup>s</sup> 15	-28°53′42″6	61.10	2.678	1.333	2.716	352	NO
CM7	M0.1073396-0.0890670	17 <sup>h</sup> 46 <sup>m</sup> 13 s 39	-28°53′27″2	44.30	1.908	1.323	2.607	350	NO
CM8	M0.1061099-0.0893484	17 <sup>h</sup> 46 <sup>m</sup> 13 <sup>s</sup> 28	-28°53′31″5	52.70	2.900	1.252	5.884	331	YES
CM9	M0.1073796-0.0820367	17 <sup>h</sup> 46 <sup>m</sup> 11 <sup>s</sup> .75	-28°53′13″9	41.15	6.005	1.210	10.429	320	NO
CM10	M0.1069128-0.0812699	17 <sup>h</sup> 46 <sup>m</sup> 11 <sup>s</sup> 51	-28°53′13″9	46.40	6.136	1.199	9.117	317	YES
CM11	M0.1054022-0.0856925	17 <sup>h</sup> 46 <sup>m</sup> 12 <sup>s</sup> 33	-28°53′26″8	53.75	1.864	1.165	3.439	308	NO
CM12	M0.1037539-0.0847109	17 <sup>h</sup> 46 <sup>m</sup> 11 <sup>s</sup> 86	-28°53′30″0	53.75	2.552	1.063	6.657	281	YES
CM13	M0.1025205-0.0844109	17 <sup>h</sup> 46 <sup>m</sup> 11 <sup>s</sup> 62	$-28^{\circ}53'33\rlap.{''}3$	53.75	1.525	1.020	1.581	270	NO

Table A2 (Continued)

ID	Maser Name	$\alpha$ (J2000)	δ (J2000)	${\rm km~s^{-1}}$	FWHM km s <sup>-1</sup>	$I_{ m peak}$ Jy b <sup>-1</sup>	Flux Jy km s <sup>-1</sup>	$_{ m K}^{T_b}$	Resolved?
CM14	M0.1086098-0.0871261	17 <sup>h</sup> 46 <sup>m</sup> 13 <sup>s</sup> 12	-28°53′19″6	59.00	8.039	0.989	8.824	261	YES
CM15	M0.1034571-0.0811550	17 <sup>h</sup> 46 <sup>m</sup> 10 <sup>s</sup> 99	-28°53′24″3	56.90	5.577	0.987	9.074	261	YES
CM16	M0.0998050-0.0797587	17 <sup>h</sup> 46 <sup>m</sup> 10 <sup>s</sup> 14	-28°53′32″9	56.90	3.739	0.945	5.708	250	NO
CM17	M0.1070237-0.0799179	17 <sup>h</sup> 46 <sup>m</sup> 11 <sup>s</sup> 21	-28°53′11″0	60.05	7.663	0.930	11.283	246	YES
CM18	M0.1080322-0.0903968	17 <sup>h</sup> 46 <sup>m</sup> 13 <sup>s</sup> 80	-28°53′27″5	41.15	4.784	0.889	7.060	235	YES
CM19	M0.1053015-0.0807328	17 <sup>h</sup> 46 <sup>m</sup> 11 <sup>s</sup> 15	-28°53′17″8	45.35	4.598	0.860	7.262	227	YES
CM20	M0.0989385-0.0806366	17 <sup>h</sup> 46 <sup>m</sup> 10 <sup>s</sup> 22	-28°53′37″2	53.75	5.362	0.855	6.528	226	YES
CM21	M0.1002794-0.0816885	17 <sup>h</sup> 46 <sup>m</sup> 10 <sup>s</sup> .66	-28°53′35″1	49.55	2.898	0.824	6.111	218	YES
CM22	M0.1051058-0.0848221	17 <sup>h</sup> 46 <sup>m</sup> 12 <sup>s</sup> 08	-28°53′26″1	52.70	3.773	0.819	5.464	216	YES
CM23	M0.1093610-0.0816478	17 <sup>h</sup> 46 <sup>m</sup> 11 <sup>s</sup> 94	-28°53′07″1	55.85	4.041	0.811	4.470	214	YES
CM24	M0.1043426-0.0831849	17 <sup>h</sup> 46 <sup>m</sup> 11 <sup>s</sup> 59	-28°53′25″4	45.35	8.092	0.730	5.279	193	YES
CM25	M0.1015946-0.0840405	$17^{h}46^{m}11 \stackrel{s}{.} 40$	-28°53′35″4	48.50	2.788	0.678	2.904	179	YES
CM26	M0.1090351-0.0814959	17 <sup>h</sup> 46 <sup>m</sup> 11 <sup>s</sup> 86	-28°53′07″8	52.70	4.308	0.668	2.702	176	NO
CM27	M0.1083018-0.0818256	17 <sup>h</sup> 46 <sup>m</sup> 11 <sup>s</sup> 84	-28°53′10″6	45.35	4.275	0.586	4.017	155	NO
CM28	M0.1074053-0.0807365	17 <sup>h</sup> 46 <sup>m</sup> 11 <sup>s</sup> .45	-28°53′11″4	47.45	4.038	0.572	3.719	151	YES
CM29	M0.1016794-0.0813032	17 <sup>h</sup> 46 <sup>m</sup> 10 <sup>s</sup> .77	-28°53′30″0	48.50	< 1.05	0.540	0.553	143	NO
CM30	M0.1987015-0.0810144	17 <sup>h</sup> 46 <sup>m</sup> 10 <sup>s</sup> 28	-28°53′38″7	43.25	< 1.05	0.504	0.365	133	NO
CM31	M0.1044869-0.0816958	17 <sup>h</sup> 46 <sup>m</sup> 11 <sup>s</sup> 26	$-28^{\circ}53'22\rlap.{''}1$	62.15	4.628	0.421	4.661	111	YES

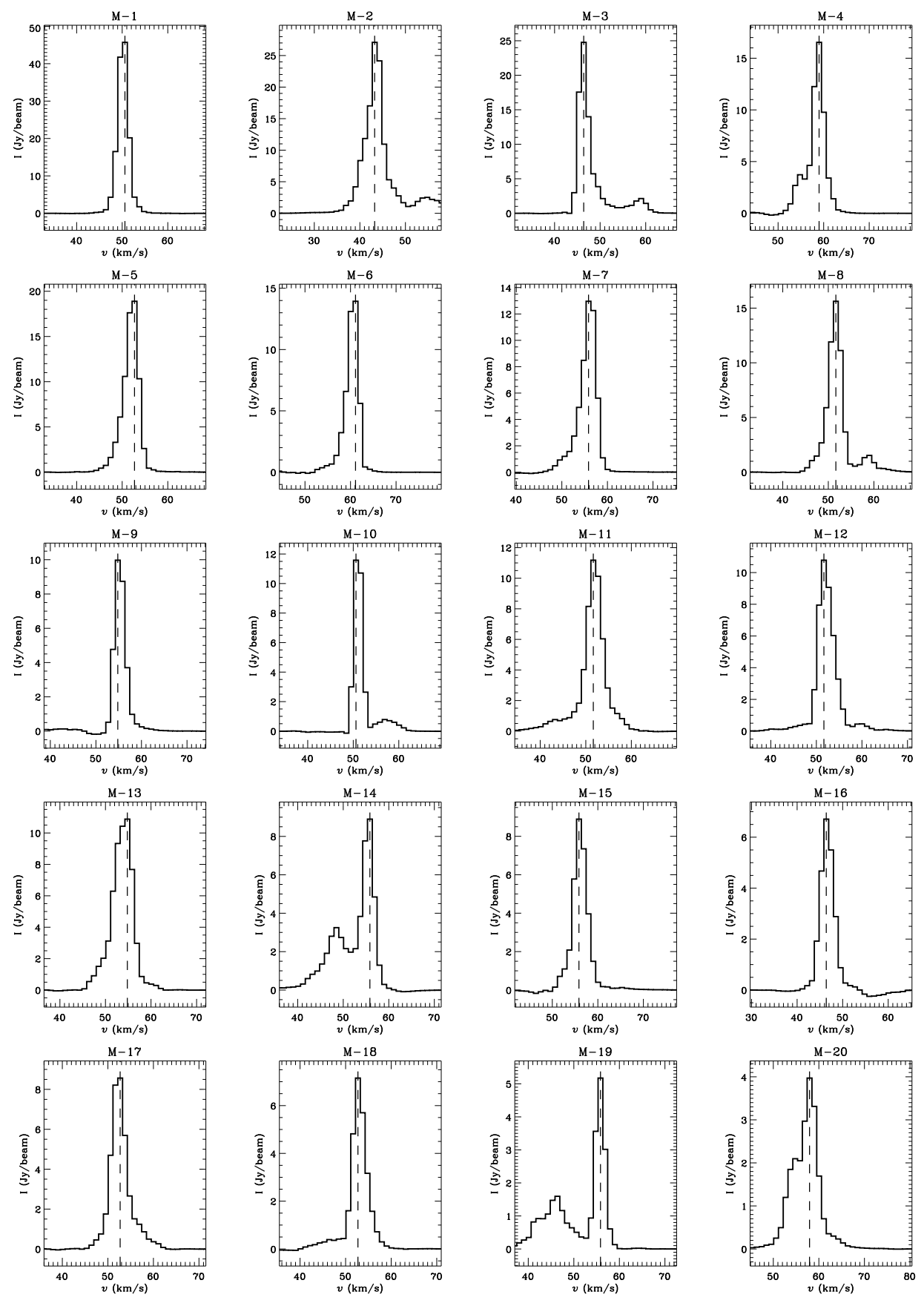


Figure A1. Spectra of detected 36 GHz CH<sub>3</sub>OH masers in M0.10-0.08.

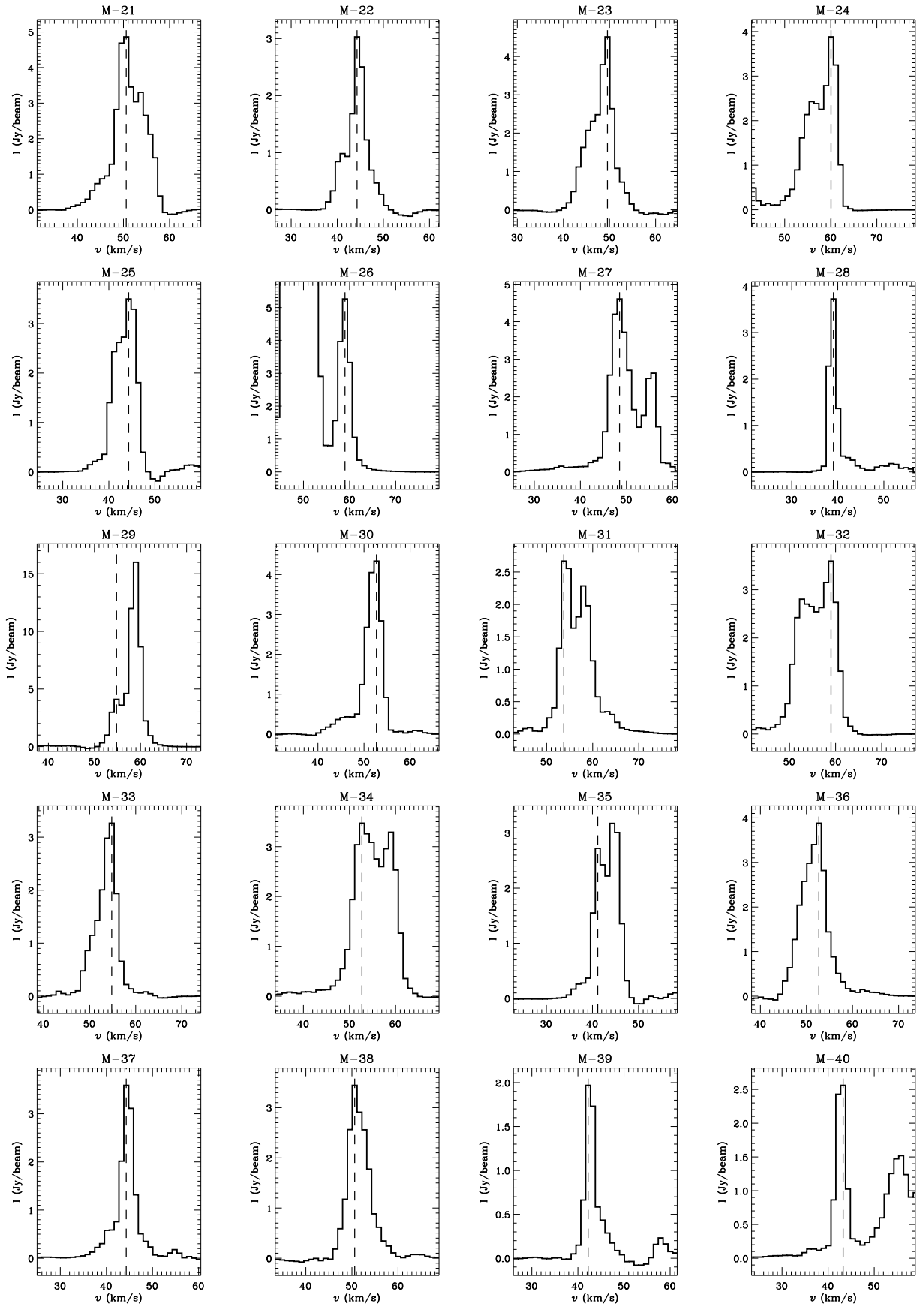


Figure A1. (Continued.)

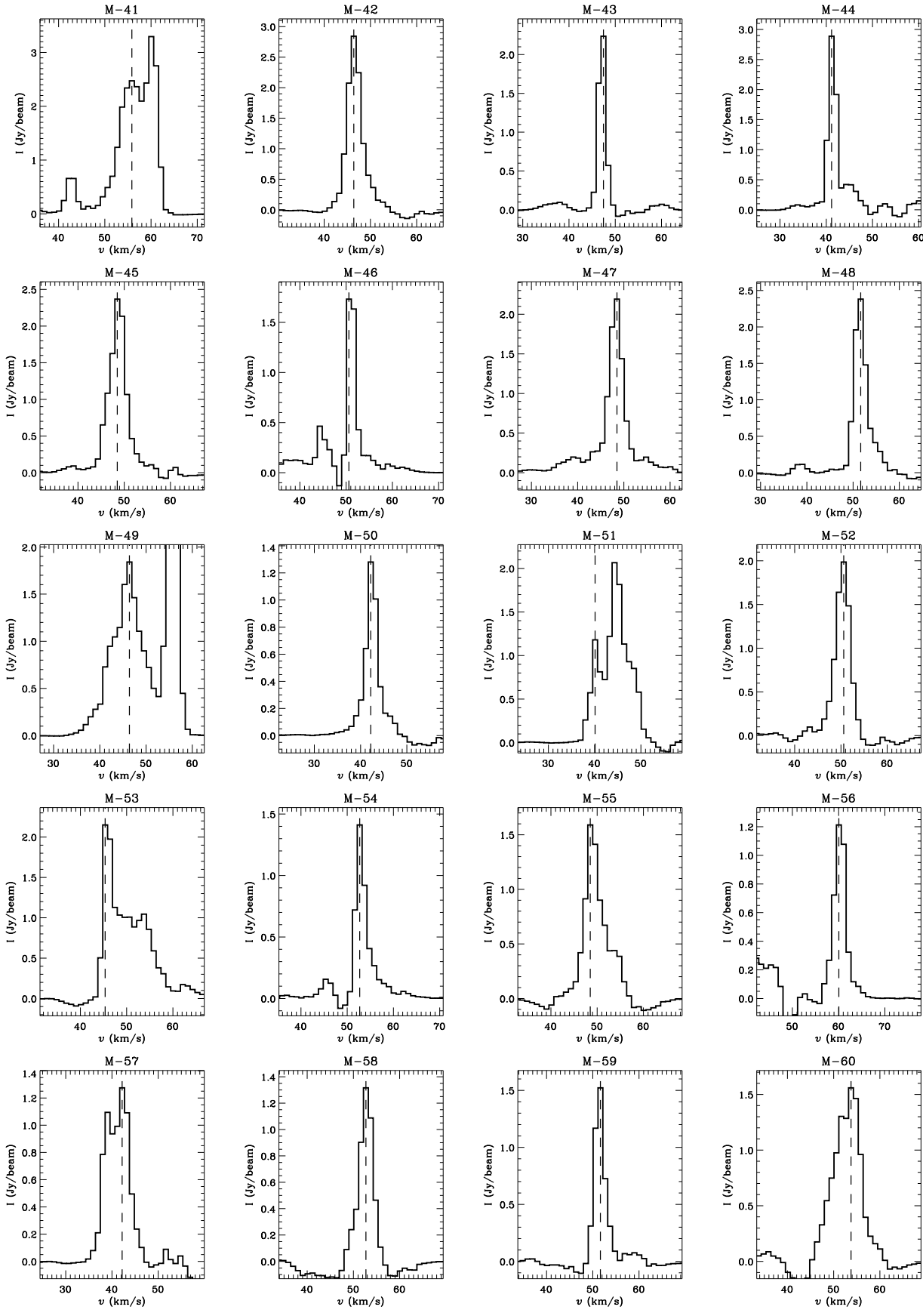


Figure A1. (Continued.)

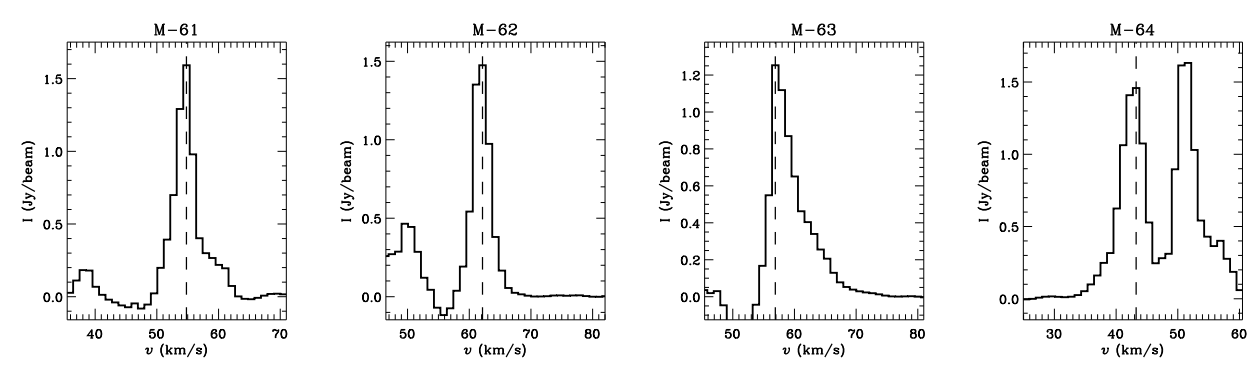


Figure A1. (Continued.)

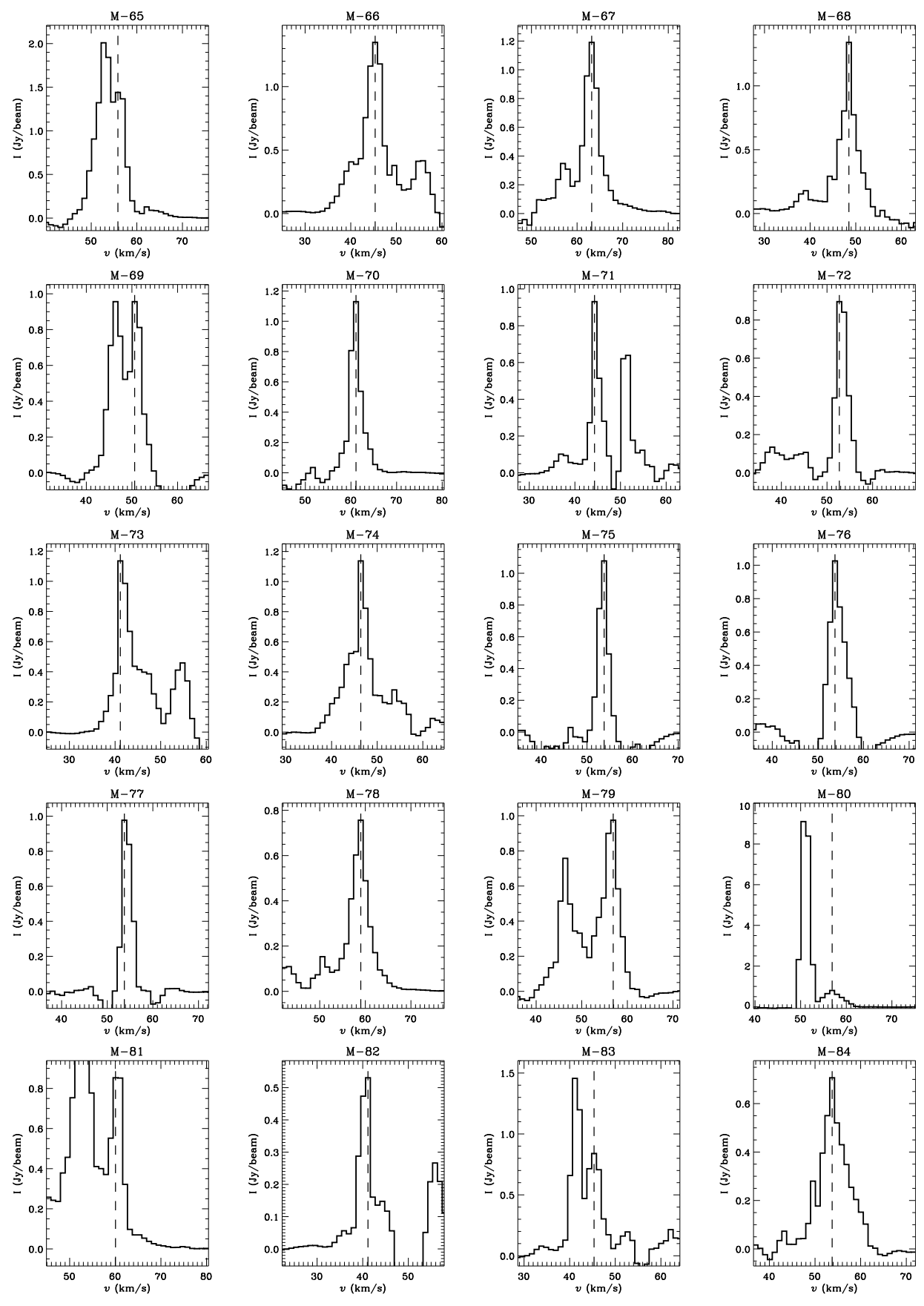


Figure A2. Maser candidates CM1(M65) to CM16(M60).

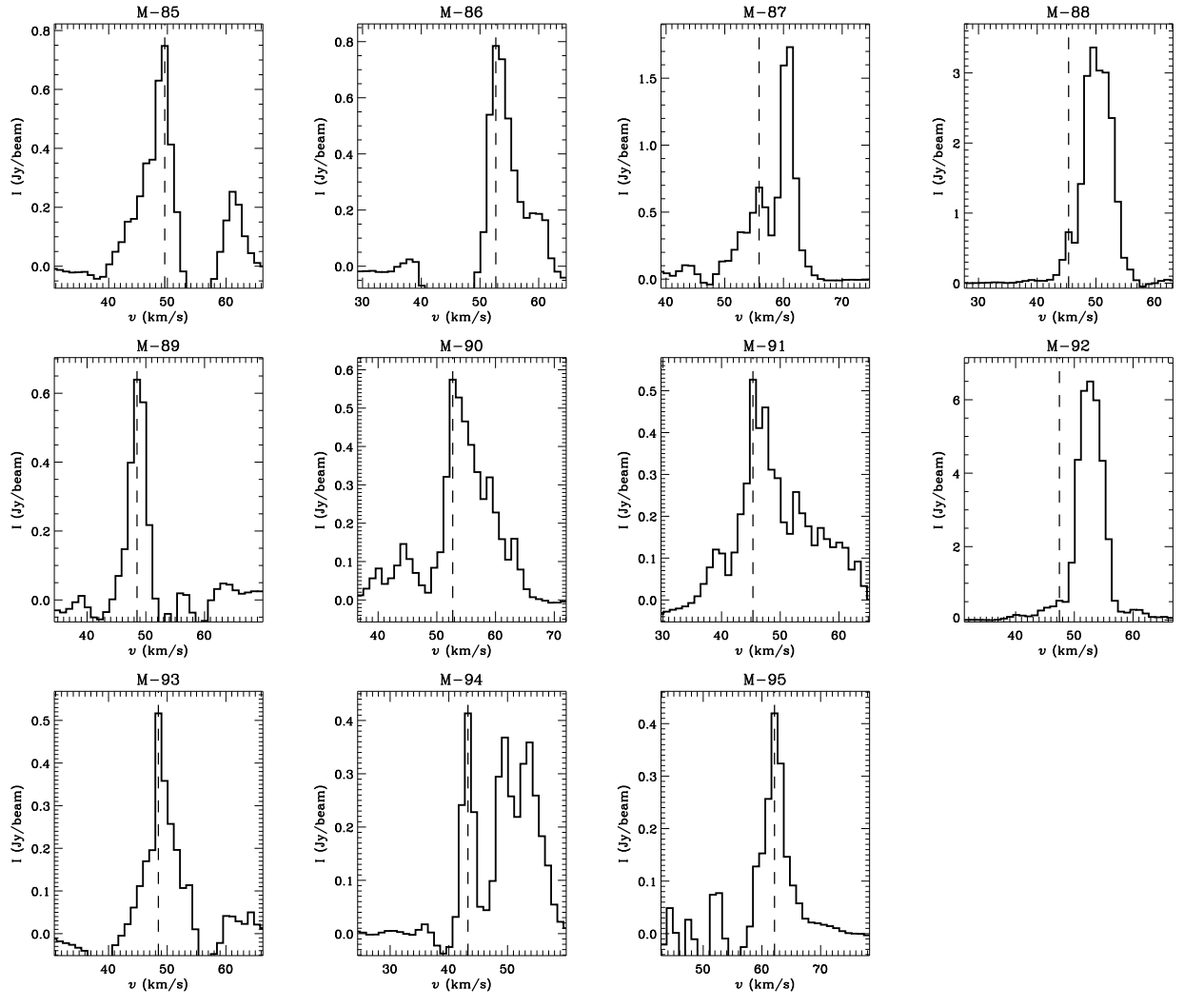


Figure A2. (Continued.)

#### **ORCID iDs**

Natalie O. Butterfield https://orcid.org/0000-0002-4013-6469

Adam Ginsburg https://orcid.org/0000-0001-6431-9633
Mark R. Morris https://orcid.org/0000-0002-6753-2066
Jürgen Ott https://orcid.org/0000-0001-8224-1956
Dominic A. Ludovici https://orcid.org/0000-0002-8631-6457

#### References

Bally, J., Stark, A. A., Wilson, R. W., & Henkel, C. 1987, ApJS, 65, 13
Battersby, C., Keto, E., Walker, D., et al. 2020, ApJS, 249, 35
Butterfield, N., Lang, C. C., Morris, M., Mills, E. A. C., & Ott, J. 2018, ApJ, 852, 11
Churchwell, E., Babler, B. L., Meade, M. R., et al. 2009, PASP, 121, 213
Chuss, D. T., Davidson, J. A., Dotson, J. L., et al. 2003, ApJ, 599, 1116
Clavel, M., Terrier, R., Goldwurm, A., et al. 2013, A&A, 558, A32
Cotton, W. D., & Yusef-Zadeh, F. 2016, ApJS, 227, 10
Cramphorn, C. K., & Sunyaev, R. A. 2002, A&A, 389, 252
Do, T., Hees, A., Ghez, A., et al. 2019, Sci, 365, 664
Fukui, Y., Iguchi, T., Kaifu, N., et al. 1977, PASJ, 29, 643
Fukui, Y., Torii, K., Ohama, A., et al. 2016, ApJ, 820, 26
Ginsburg, A., Henkel, C., Ao, Y., et al. 2016, A&A, 586, A50
Ginsburg, A., & Mirocha, J. 2011, PySpecKit: Python Spectroscopic Toolkit, Astrophysics Source Code Library, ascl:1109.001

```
Ginsburg, A., Sokolov, V., de Val-Borro, M., et al. 2022, AJ, 163, 291
Guan, Y., Clark, S. E., Hensley, B. S., et al. 2021, ApJ, 920, 6
Güsten, R., Walmsley, C. M., & Pauls, T. 1981, A&A, 103, 197
Handa, T., Sakano, M., Naito, S., Hiramatsu, M., & Tsuboi, M. 2006, ApJ,
   636, 261
Hatchfield, H. P., Battersby, C., Keto, E., et al. 2020, ApJS, 251, 14
Haworth, T. J., Tasker, E. J., Fukui, Y., et al. 2015, MNRAS, 450, 10
Henshaw, J. D., Longmore, S. N., Kruijssen, J. M. D., et al. 2016, MNRAS,
   457, 2675
International Consortium Of Scientists 2011, CASA: Common Astronomy
   Software Applications, Astrophysics Source Code Library, ascl:1107.013
Jones, P. A., Burton, M. G., Cunningham, M. R., et al. 2012, MNRAS,
   419, 2961
Kauffmann, J., Pillai, T., Zhang, Q., et al. 2017, A&A, 603, A89
Krieger, N., Ott, J., Beuther, H., et al. 2017, ApJ, 850, 77
Kruijssen, J. M. D., Dale, J. E., & Longmore, S. N. 2015, MNRAS, 447, 1059
Ludovici, D. A., Lang, C. C., Morris, M. R., et al. 2016, ApJ, 826, 218
Mauersberger, R., Henkel, C., Wilson, T. L., & Walmsley, C. M. 1986, A&A,
   162, 199
McMullin, J. P., Waters, B., Schiebel, D., Young, W., & Golap, K. 2007, in
   ASP Conf. Ser. 376, Astronomical Data Analysis Software and Systems
   XVI, ed. R. A. Shaw, F. Hill, & D. J. Bell (San Francisco, CA: ASP), 127
Menten, K. M. 1991, ApJL, 380, L75
Mills, E. A. C., & Battersby, C. 2017, ApJ, 835, 76
Mills, E. A. C., Butterfield, N., Ludovici, D. A., et al. 2015, ApJ, 805, 72
Mills, E. A. C., Ginsburg, A., Clements, A. R., et al. 2018b, ApJL, 869, L14
Mills, E. A. C., Ginsburg, A., Immer, K., et al. 2018a, ApJ, 868, 7
Mills, E. A. C., Lang, C. C., Morris, M. R., et al. 2014, in ÎAU Symp. 303, The
   Galactic Center: Feeding and Feedback in a Normal Galactic Nucleus, ed.
```

```
L. O. Sjouwerman, C. C. Lang, & J. Ott (Cambridge: Cambridge Univ. Press), 139

Mills, E. A. C., & Morris, M. R. 2013, ApJ, 772, 105

Molinari, S., Bally, J., Noriega-Crespo, A., et al. 2011, ApJL, 735, L33

Molinari, S., Swinyard, B., Bally, J., et al. 2010, PASP, 122, 314

Morimoto, M., Kanzawa, T., & Ohishi, M. 1985, ApJL, 288, L11

Ponti, G., Terrier, R., Goldwurm, A., Belanger, G., & Trap, G. 2010, ApJ, 714, 732

Sawada, T., Hasegawa, T., Handa, T., & Cohen, R. J. 2004, MNRAS, 349, 1167

Sjouwerman, L. O., Pihlström, Y. M., & Fish, V. L. 2010, ApJL, 710, L111

Sofue, Y. 1995, PASJ, 47, 527

Sunyaev, R., & Churazov, E. 1998, MNRAS, 297, 1279
```

```
Takahira, K., Tasker, E. J., & Habe, A. 2014, ApJ, 792, 63
Terrier, R., Clavel, M., Soldi, S., et al. 2018, A&A, 612, A102
Torii, K., Hattori, Y., Hasegawa, K., et al. 2017, ApJ, 835, 142
Tsuboi, M., Tadaki, K.-I., Miyazaki, A., & Handa, T. 2011, PASJ, 63, 763
Tsuboi, M., Ukita, N., & Handa, T. 1997, ApJ, 481, 263
Williams, J. P., de Geus, E. J., & Blitz, L. 1994, ApJ, 428, 693
Williams, J. P., de Geus, E. J., & Blitz, L. 2011, Clumpfind: Determining
Structure in Molecular Clouds, Astrophysics Source Code Library,
ascl:1107.014
Yusef-Zadeh, F., Cotton, W., Viti, S., Wardle, M., & Royster, M. 2013, ApJL,
764, L19
Zylka, R., Guesten, R., Henkel, C., & Batrla, W. 1992, A&AS, 96, 525
```